

Fabrication of Nano-Structured Palladium Membranes

By Yue Hua (Hope) Tan

A thesis submitted to the Faculty of Graduate Studies and Research in
partial fulfillment of the requirements for the degree of Master of
Engineering

Department of Mining and Materials Engineering
McGill University, Montreal, Quebec, Canada
January, 2009

© By Yue Hua (Hope) Tan, 2009

ABSTRACT

Palladium, being impermeable to all gases except hydrogen, has been widely studied for hydrogen extraction in recent years. The specific surface area of the membrane is an important factor affecting the hydrogen permeation rate. How to obtain a palladium membrane with a high specific surface area is a great challenge for material scientists. In this study, a novel template-assisted technique was used to prepare nano-structured palladium membranes with a greatly increased hydrogen contacting surface.

First, the anodic aluminum oxide (AAO) template was fabricated by anodizing electro-deposited aluminum film and commercially available aluminum foil. The template was then filled with palladium using the electrochemical and the sputter deposition techniques. Various factors affecting the preparation of the palladium membrane were analyzed and optimized. The preliminary hydrogen-permeation experiments clearly showed that the nano-structured palladium membrane is a promising candidate for the application of hydrogen separation.

RÉSUMÉ

Le palladium, étant imperméable à tous les gaz à l'exception de l'hydrogène, a été largement étudié pour l'extraction d'hydrogène dans les dernières années. La surface spécifique de la membrane est un facteur important qui affecte le taux de perméabilité d'hydrogène. Un grand défi pour la communauté scientifique est d'obtenir une membrane en palladium avec une surface spécifique élevée. Dans cette étude, une nouvelle technique utilisant une matrice ordonnée a été employée pour préparer des membranes de palladium nano-structurées avec une surface de contact avec l'hydrogène considérablement accrue.

Tout d'abord, l'oxyde d'aluminium anodique (OAA) a été fabriqué en anodisant une couche d'aluminium électro-déposée et un papier d'aluminium commercial. Puis, la matrice d'OAA a été remplie de palladium utilisant la technique électrochimique et la technique par pulvérisation. De divers facteurs affectant la préparation de la membrane de palladium ont été analysés et optimisés. Les expériences préliminaires de la perméabilité d'hydrogène ont clairement prouvé que de telles membranes de palladium sont un candidat prometteur pour l'application de la séparation d'hydrogène.

ACKNOWLEDGEMENT

First I would like to offer my heartfelt thanks to my supervisor, Professor Jerzy A. Szpunar, who has provided me with guidance, inspiration, scholarly support and constant encouragement throughout my Master's studies. His keen aptitude for research and his scientific approach to problems have played a pivotal role in my learning and in the completion of this work.

I would also like to express my appreciation to Dr. Shanqiang Wu of the H₂ TEC Company for assisting me in the completion of the hydrogen permeation tests; and to Mr. Slavek Poplaski for his assistance with the XRD and texture measurements and the other experiments.

Thank you to all the members of the texture lab, including research fellow Dr. Marwan Azzi, Dr. Zhongliang Shi, Dr. Wen Qin, Dr. Hualong Li, Mr. Arafin Muhammad, Mr. Minhui Huang, and Miss Emilie Hsu. I have enjoyed sharing the cheerful atmosphere of Professor Szpunar's group.

Finally, I wish to express my gratitude to my family and especially my son Yingpeng Cheng for his continuous support and help during my studies at McGill.

TABLE OF CONTENTS

ABSTRACT	i
RÉSUMÉ	ii
ACKNOWLEDGEMENT	iii
TABLE OF CONTENTS	iv
LIST OF FIGURES	vii
LIST OF TABLES	xi
CHAPTER 1 Introduction.....	1
CHAPTER 2 Literature Review	3
2.1 Introduction.....	3
2.2 Palladium membranes for hydrogen permeation	4
2.2.1 Mechanism for hydrogen permeation (Sievert's Law)	4
2.2.2 Gas permeation in porous medium	6
2.2.3 Selectivity and stability.....	7
2.2.4 Resistance models for composite type palladium membranes.....	8
2.2.5 Different type composite palladium membranes	10
2.3 Electro-deposition of aluminum in non-aqueous solution	13
2.3.1 Tetrahydrofuran (THF) solution for electroplating aluminum.....	14
2.3.2 Reaction of the solvent and the solutes in THF	14
2.3.3 Species of aluminum complex ions in THF solution.....	15
2.3.4 Effect of water in the solution.....	15
2.3.5 Fundamental of electro-deposited aluminum in THF solution	16
2.4 Formation of anodic aluminum oxide (AAO) template.....	19
2.4.1 Electrochemical reaction in AAO	19

2.4.2 Pore structure in anodic aluminum oxide membranes	20
2.4.3 Mechanism of self-ordered pore formation	20
CHAPTER 3 Fabrication of Al films by electroplating.....	23
3.1 Experimental procedure	23
3.1.1 Solution preparation.....	24
3.1.2 Electro-deposition of aluminum films	25
3.1.3 Characterization method of as-deposited aluminum films	25
3.2 Optimization of the fabrication process in electroplating aluminum films	26
3.2.1 Factors affecting covering power.....	26
3.2.2 Factors affecting microstructure of as-deposited aluminum films.....	33
3.3.3 Crystalline structure of as-deposited films.....	39
3.3.4 Texture of as-deposited films.....	41
3.3 Summary	42
CHAPTER 4 Fabrication of AAO template.....	44
4.1 Experimental procedure	44
4.1.1 AAO template fabricated on aluminum foils	45
4.1.2 AAO template fabricated on as-deposited aluminum films	46
4.1.3 AAO template fabricated by anodizing electro-polished aluminum.....	47
4.2 Results and discussion	48
4.2.1 Factors affecting on the formation of AAO template	48
4.2.2 Removal of barrier layer on the bottom of the as-prepared AAO template.....	50
4. 2.3 Electrochemical behavior in anodization of as-deposited aluminum films	51
4. 2.4 Morphology of anodized as-deposited aluminum films	55

LIST OF FIGURES

Figure 1 Illustration of increased contacting surface area for nano-structured palladium membrane.....	2
Figure 2 Mechanism of hydrogen permeation across palladium membrane [5].....	5
Figure 3 Schematic drawings depicting Poiseuille and Knudsen flow [6].....	6
Figure 4 Schematic diagram of gas permeation via composite Pd membrane.....	8
Figure 5 Schematic diagram of gas permeation through composite Pd membrane with pinholes and modified/diffusion resistance block.....	9
Figure 6 Hydrogen fluxes of palladium membranes as a function of temperature...	13
Figure 7 Structures of aluminate species possibly present in the hydride bath [23]...	15
Figure 8 Schematic diagram of porous oxide film structure [7].....	20
Figure 9 Schematic diagram of self-organized formation of pore structure.....	22
Figure 10 SEM images of as-deposited Al obtained in solution $\text{AlCl}_3 = 0.60 \text{ mol/l}$ (at constant $\text{LiAlH}_4 = 0.30 \text{ mol/l}$)	28
Figure 11 SEM images of as-deposited Al obtained in solution $\text{AlCl}_3 = 0.94 \text{ mol/l}$ (at constant $\text{LiAlH}_4 = 0.30 \text{ mol/l}$)	28
Figure 12 SEM images of as-deposited Al obtained in solution $\text{AlCl}_3 = 1.18 \text{ mol/l}$ (at constant $\text{LiAlH}_4 = 0.30 \text{ mol/l}$)	29
Figure 13 SEM images of as-deposited Al obtained in solution $\text{LiAlH}_4 = 0.29 \text{ mol/l}$ (at constant $\text{AlCl}_3 = 0.58 \text{ mol/l}$)	30
Figure 14 SEM images of as-deposited Al obtained in solution $\text{LiAlH}_4 = 0.19 \text{ mol/l}$ (at constant $\text{AlCl}_3 = 0.58 \text{ mol/l}$).....	30

Figure 15 SEM images of as-deposited Al obtained in solution $\text{LiAlH}_4 = 0.15 \text{ mol/l}$ (at constant $\text{AlCl}_3 = 0.58 \text{ mol/l}$)	31
Figure 16 Schematic graph of the influence of AlCl_3 concentration on covering power	32
Figure 17 Microstructures obtained from as-deposited aluminum coatings	34
Figure 18 Schematic illustration of the mechanism of formation of different microstructures	37
Figure 19 Coating thickness vs. potential obtained with $\text{AlCl}_3:\text{LiAlH}_4 = 4:1$	37
Figure 20 Coating thickness vs. potential obtained with $\text{AlCl}_3:\text{LiAlH}_4 = 3:1$	38
Figure 21 XRD pattern obtained on as-deposited Al coating from normal scan ($\text{AlCl}_3:\text{LiAlH}_4 = 3:1$ in Al total concentration 1.24 mol/l)	40
Figure 22 XRD pattern obtained on as-deposited Al coating obtained from grazing angle at 1.5° ($\text{AlCl}_3:\text{LiAlH}_4 = 3:1$ in Al total concentration 1.24 mol/l)	40
Figure 23 XRD patterns of aluminum coating obtained in solution $\text{AlCl}_3:\text{LiAlH}_4 = 4:1$ in total Al concentration 1.48 mol/l under normal and grazing angle mode	41
Figure 24 Pole figures (111), (200), (220) of as-deposited aluminum coating with $\text{AlCl}_3:\text{LiAlH}_4 = 3:1$ in total Al concentration of 1.24 mol/l	41
Figure 25 Pole figures (111), (200), (220) of as-deposited aluminum coating with $\text{AlCl}_3:\text{LiAlH}_4 = 4:1$ in total Al concentration of 1.48 mol/l	42
Figure 26 Schematic illustration of anodizing device	46
Figure 27 Relationship between anodizing time and thickness of AAO template	48
Figure 28 Relationship between anodizing rate and concentration and applied voltage	49

Figure 29 SEM image of AAO in 0.6 M oxalic acid solution	49
Figure 30 Pore bottom opening in a 5 wt. % H ₃ PO ₄ solution	50
Figure 31 XRD pattern of AAO template	50
Figure 32 Current density vs. time during anodization of as-deposited 9 μm aluminum	51
Figure 33 SEM image of template fabrication with “burning”	54
Figure 34 Current density vs. time during anodization of as-deposited 6 μm aluminum	54
Figure 35 Current density vs. time during anodization of as-deposited 15 μm aluminum	55
Figure 36 Schematic illustration of two-step anodization pre-pattern process.....	56
Figure 37 SEM image of anodizing as-deposited aluminum at 10 V.....	57
Figure 38 Template obtained after pore widening in 5 wt% H ₃ PO ₄	57
Figure 39 SEM images of anodizing as-deposited aluminum at 30 V	58
Figure 40 SEM image of anodizing as-deposited aluminum at 40 V.....	59
Figure 41 SEM image of the cross section of as-deposited aluminum sample.....	60
Figure 42 Schematic illustration of obtaining ordered pore in anodization process	60
Figure 43 SEM images of template obtained by anodizing electro-polished aluminum	61
Figure 44 SEM cross section image of anodized electro-polished as-deposited Al	61
Figure 45 Template from as-deposited aluminum after pore widening	62

Figure 46 Schematic diagram of experimental setup for hydrogen permeation test	65
Figure 47 Schematic illustrations of hydrogen permeation cell and inside sealing...	65
Figure 48 Schematic sketch of palladium membrane sealing in hydrogen permeation	66
Figure 49 Schematic illustration of self-sealing palladium membrane fabrication...	67
Figure 50 Schematic graph of fabrication process of electro-deposited Pd membrane	68
Figure 51 SEM images of removed nano-structured Pd membrane embedded in AAO	69
Figure 52 SEM images of nano-structured palladium membrane bottom view	69
Figure 53 EDS spectrum and SEM image of freed electro-deposited Pd membrane	70
Figure 54 SEM images of unevenly electro-deposited palladium membrane	70
Figure 55 SEM image of cracking in electroplated Pd membrane at high potential...	71
Figure 56 SEM image of palladium membrane fabrication with deposition time.....	72
Figure 57 EDS spectrums of Pd membranes after 40 and 50 minutes sputtering.....	73
Figure 58 Hydrogen permeation rate vs. temperature performed on sputtered Pd ...	74
Figure 59 SEM image of sputtered Pd membrane after hydrogen permeation.....	75
Figure 60 XRD pattern for sputtered palladium sample after hydrogen permeation	75

LIST OF TABLES

Table 1 Typical anodization conditions for various electrolytes	22
Table 2 Solution Preparation with constant AlCl_3 concentration.....	25
Table 3 Solution Preparation with constant LiAlH_4 concentration	25
Table 4 Summary of the covering power at different electroplating conditions	31
Table 5 Microstructure of as-deposited aluminum films under different concentrations and different potentials.....	35

CHAPTER 1 Introduction

Hydrogen is not only an environmentally clean energy resource, but also an important raw material and product in chemical industries. Environmental concerns and energy crisis have led to continuously increased global interest in the development of a hydrogen economy. Hydrogen separation and purification are essential processes when hydrogen is applied in low temperature fuel cells and chemical plants. As far as hydrogen separation and purification are concerned, palladium is outstanding due to its good selectivity, permeability and stability.

Starting in the 1960s, many studies were conducted on self-supported dense metallic membranes, which had a thickness between 100 and 200 microns. Although these membranes have a high selectivity, their low hydrogen flux and high material cost make them impractical in industrial applications.

Since the permeation rate of hydrogen is inversely proportional to membrane thickness, an effective solution for the improvement of permeation rate is to reduce membrane thickness. In order to ensure a reasonable permeation flux and lower the material cost, composite-type palladium membranes have been developed. This kind of palladium membranes consists of a thin palladium layer with a thickness of 4 to 25 microns deposited on porous supports. The thermal stability and mechanical strength of a film are directly related to film thickness. A certain membrane thickness is therefore needed to provide the necessary mechanical strength and thermal stability. How to increase the hydrogen permeation rate and obtain pinhole-free palladium membranes are the major concerns of researchers.

The mechanism of hydrogen permeation through palladium membranes shows that hydrogen permeation consists of surface adsorption and desorption processes as

well as a bulk-diffusion process. At low temperatures, the surface processes are rate-controlling steps. Therefore, increasing the surface area will eventually speed up the hydrogen permeation rate. In addition, low temperature operating conditions have significant and practical application in industries. In this study, a novel solution is put forward to the existing problem, that is, to develop a nano-structured palladium membrane. With the same geometric dimensions, the hydrogen permeation rate may be increased due to the substantial increase of hydrogen-contact with the surface area, as illustrated in Figure 1.

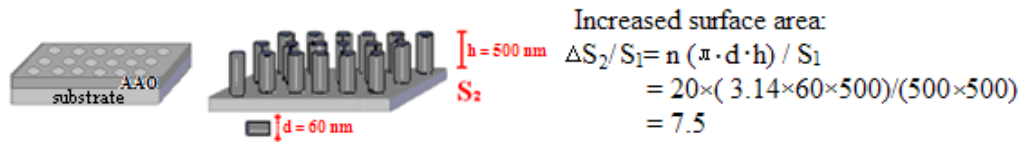


Figure 1 Illustration of increased contacting surface area for nano-structured palladium membrane

The overall objective of this project is therefore to develop nano-structured palladium membranes. In this thesis, the fabrication of nano-structured palladium membranes will be achieved using a template assisted method. The anodization of aluminum needs to be investigated firstly. This anodized aluminum will then be applied as templates for nano-structured palladium membrane fabrication. The primary objectives of this present work are: (a) to establish and optimize a template fabrication process by anodizing electroplated aluminum; and (b) to fabricate nano-structured palladium membranes by a template assisted method.

CHAPTER 2 Literature Review

2.1 Introduction

Increased public awareness of global warming and increasing environmentally clean energy demands have led to the advancement of new energy sources. Hydrogen, the lightest chemical element in universe, has the highest energy content per unit weight of any known elements (143 kJ/g). Unlike petroleum, it can be easily generated using renewable energy sources (i.e. water, wind and solar energy). It forms non-polluting, harmless byproduct during usage, and is an environmentally friendly alternative to conventional fossil fuels. When hydrogen is used in fuel cells, the efficiency can be up to about 50-60%, which is more than twice that of a thermal cycle. In addition, hydrogen can be employed as a fuel in internal combustion engines. As a clean energy source, hydrogen has been of great interest in recent decades and is an attractive energy source for the future. Over the next several decades, a shift away from the fossil fuel economy is expected towards a much cleaner hydrogen economy. However, hydrogen must be extracted and purified before use. Palladium and its alloys are the most promising candidates for hydrogen separation and purification due to their good hydrogen permeability and selectivity.

Much research has been done on palladium membranes for hydrogen separation and purification. The earliest palladium membranes studied for hydrogen separation and purification was self-supported dense metallic membranes having a thickness of 100 to 200 μm , made by conventional metallurgical processes. As the hydrogen flux is inversely proportional to the membrane thickness, a thick membrane is a poor separator. In addition, palladium is too expensive to be used as a bulk material. Thinner palladium membranes are favored in industrial applications. Therefore, the

second category, composite-type palladium membranes, has been developed. These membranes consist of thin palladium films deposited on porous substrates that can provide a certain mechanical strength to the membranes. This chapter will mainly discuss the hydrogen selectivity and diffusion mechanisms in palladium, and at the same time, give an overview of literature for two types of palladium membranes. Following this, the theories related to template fabrication process will be presented.

2.2 Palladium membranes for hydrogen permeation

2.2.1 Mechanism for hydrogen permeation (Sievert's Law)

Hydrogen can permeate through many pure metals, including palladium, vanadium, tantalum, niobium and titanium. All of these, with the exception of palladium, are unstable. Poisoning of the membrane surface by oxidation or sulfur deposition from traces of hydrogen sulfide often take place and make these metals unsuitable for applications.

When hydrogen gas permeates through a dense palladium membrane, the solution-diffusion model, as illustrated in Figure 2, can be used to illustrate this process. The mechanism occurs in 6 steps [5] as follows: First, hydrogen molecules are captured by the palladium atoms on the surface of palladium membrane. Then, the captured hydrogen molecules are dissociated and adsorbed on the Pd membrane surface: thus, atomic hydrogen is formed on the surface. In the third step, atomic hydrogen is dissolved in the bulk layer of palladium by the pressure gradient, and diffuses through the bulk palladium films. When hydrogen atoms reach the opposite surface of palladium membrane, the atomic hydrogen forms molecules and become desorbed.

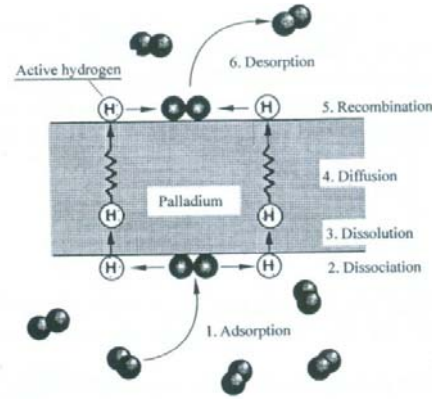


Figure 2 Mechanism of hydrogen permeation across palladium membrane [5]

When hydrogen permeates in a dense palladium membrane, the above mechanism of hydrogen permeation is generally assumed. It involves both surface processes (step 1, step 2, step 5, and step 6) and a bulk-diffusion process (step 3, step 4). It was reported by R.W. Baker [8] that at high temperatures ($>300\text{ }^{\circ}\text{C}$), the surface sorption and dissociation processes are fast; the rate-controlling step is the diffusion of atomic hydrogen through the palladium metal lattice, which can be expressed as follows:

$$J = F_{p1} (P_{H_{2,f}}^n - P_{H_{2,p}}^n) = \frac{Q}{l} (P_{H_{2,f}}^n - P_{H_{2,p}}^n) \quad (2.1)$$

where J represents hydrogen permeation flux ($\text{mol}/\text{m}^2\cdot\text{s}$), F_{p1} is a premultiplication factor, and n is a constant. Q , the permeability of hydrogen through a membrane ($\text{mol}/\text{m}\cdot\text{s}\cdot\text{Pa}^n$), which is the product of diffusivity and solubility, while l is the membrane thickness, and $P_{H_{2,f}}$ and $P_{H_{2,p}}$ are the partial pressures of hydrogen on the feed and permeation sides, respectively. For a bulk-diffusion process, $n = 0.5$. The hydrogen flux can be described by Sieverts' Law

$$J = \frac{Q}{l} (\sqrt{P_{H_{2,f}}} - \sqrt{P_{H_{2,p}}}) = DS (\sqrt{P_{H_{2,f}}} - \sqrt{P_{H_{2,p}}})/l \quad (2.2)$$

where D and S are the hydrogen diffusion coefficient and the hydrogen solubility

constant, respectively. While at low temperatures, the surface processes are the rate-controlling steps, any increase of surface area will speed up the hydrogen permeation rate.

2.2.2 Gas permeation in porous medium

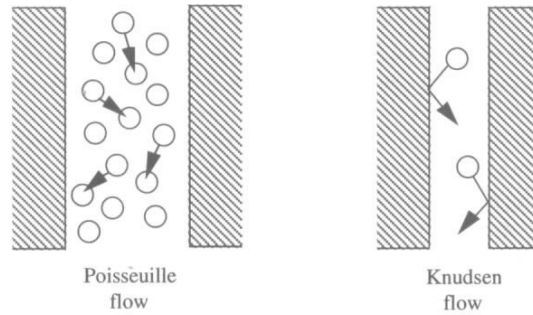


Figure 3 Schematic drawings depicting Poiseuille and Knudsen flow [6]

The gas permeation mechanism in a porous medium can be described by Poiseuille flow (or viscous flow), or by Knudsen diffusion, as shown in Figure 3. The relative contribution of Knudsen diffusion to the overall transport rate depends on the Knudsen number, K_n , which is defined as the ratio of mean free path of the gas molecules λ [nm] to the pore radius of the medium r [nm] [9], that is,

$$K_n = \lambda / r \quad (2.3)$$

$$\lambda = \left(\frac{16\mu}{5\pi P_{ave}} \right) \left(\frac{\pi RT}{2M} \right) \quad (2.4)$$

where P_{ave} [Pa] is the average pressure across the medium, μ [$N \cdot s/m^2$] is the gas viscosity, T is the absolute temperature, M [g/mol] is the gas molecular mass, and R [J/mol·K] is the universal gas constant. Under certain experimental conditions, λ is constant. The Knudsen number K_n , therefore, mainly depends on the pore radius.

If the Knudsen number is much larger than unity, that is, $K_n \gg 1$, the gas molecules collide with the pore wall much more frequently than with each other.

Under this condition, gas transport mechanism can be described as Knudsen flow, as illustrated in Figure 3. If, on the other hand, the Knudsen number is much smaller than unity, Poiseuille flow mechanism is dominant. In the range of $0.01 < K_n < 10$, the transition from Knudsen to Poiseuille flow occurs.

2.2.3 Selectivity and stability

The high stability and high selectivity of the palladium membranes are the two major attractions of these membranes. Usually, hydrogen permeation through the dense membranes increases with increasing temperature. However, as the operating temperature increases, the use of the membranes in industrial applications becomes increasingly inconvenient. The selectivity coefficient (α_{ij}^*), or ideal separation factor, defined as the ratio of permeability of two gases (pure hydrogen and non-permeable gas Ar, N₂, or He, etc) is expressed as follows:

$$\alpha_{ij}^* = F_{p,i} / F_{p,j} \quad (2.5)$$

Theoretically, composite membranes should have an infinite selectivity, given that these membranes are only permeable to hydrogen. However, the presence of cracks and pinholes can permeate unwanted species, lowering the purity of hydrogen, and thus decreasing the selectivity.

Cracking of membrane layers can be results of the formation of pinholes and might be related to specific operation conditions, or interactions between the support and palladium layer, or phase transformation process. Low temperature of operation will definitely reduce the interaction between the support and membrane, and make the palladium membrane more stable.

2.2.4 Resistance models for composite type palladium membranes

The resistance model, as illustrated in Figure 4, can be used to discuss the influence of resistance of each membrane component to overall hydrogen transport. According to this model, the permeation of hydrogen through the composite membranes is analogous to a flow of electricity through the resistor series R_{Pd} and R_s , while the hydrogen flux corresponds to the current and the pressure drop corresponds to the voltage drop [9]. When a thin palladium membrane is deposited on a porous substrate, hydrogen permeation resistance comes both from the thin palladium layer and the support. Mathematically, the hydrogen permeation flux, J_{H_2} , is related to the mass transfer resistance of the thin, dense palladium top layer (R_{Pd}) and of the support (R_s). Assuming the same substrate is used, the hydrogen flux through the bulk palladium layer of composite membrane will be determined by the palladium membrane only.

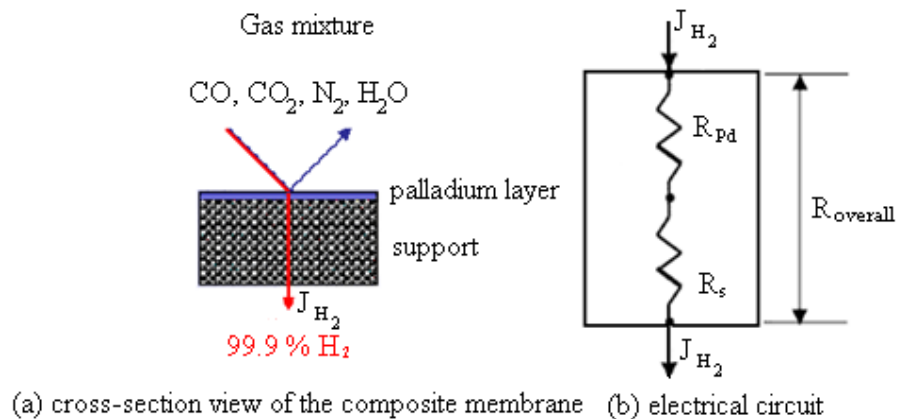


Figure 4 Schematic diagram of gas permeation via composite Pd membrane

However, if pinholes or cracks exist in the top palladium layer, or if a diffusion layer is produced between the top palladium layer and metal supporting substrate, or if a modifier layer is used, the hydrogen transport can be more analogous, as illustrated in Figure 5.

The hydrogen permeation flux is related to the mass transfer resistance of the dense palladium layer (R_1), of the pinhole (R_2), of the modified/barrier layer (R_3) and of the substrate (R_4) [10]. It can be expressed as follows

$$J_{H_2} = \frac{1}{1(1/R_1 + 1/R_2) + R_3 + R_4} \quad (2.6)$$

If the resistance in the modified/barrier layer (R_3) and the porous substrate (R_4) are negligible (the same substrate), the hydrogen flux can be written as

$$J_{H_2} \propto 1/R_1 + 1/R_2 \quad (2.7)$$

Therefore, in the case where pinholes or cracks exist in the palladium layer, the hydrogen gas permeates through the dense palladium layer and the pinholes, whereas impurities in the mixture gas can only permeate through pinholes. The flux of impurities decreases slightly with temperature due to Knudsen flow.

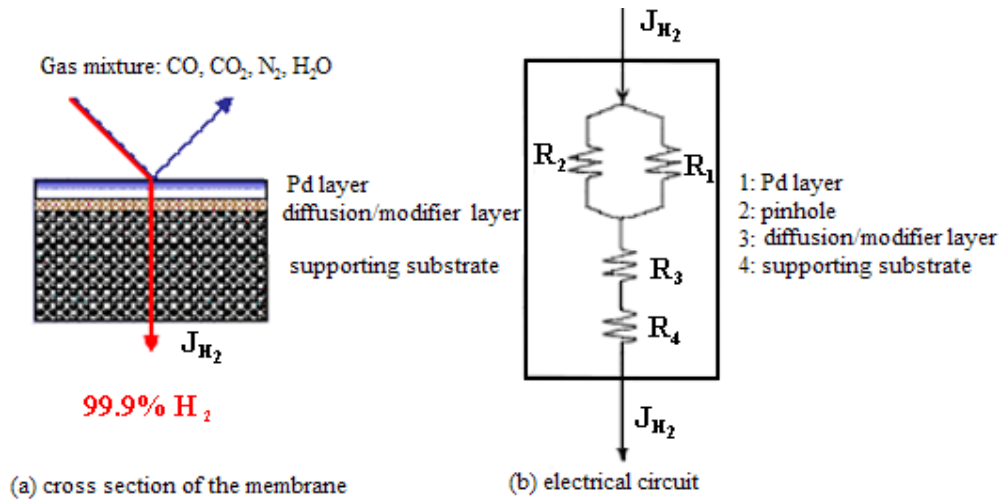


Figure 5 Schematic diagram of gas permeation through composite palladium membrane with pinholes and modified/diffusion resistance block

It can be concluded that in order to fabricate a composite membrane with high permeation flux and high selectivity, the resistance of the dense palladium layer (R_1) should be reduced, while the resistance of the pinhole (R_2) should be increased. The

resistance of the dense palladium layer (R_1) is determined by the film thickness (where the diffusion process is rate-determining) and surface area (the surface processes are rate-determining). The resistance of pinholes (R_2) can be increased by reducing the number of pinholes, as well as the pinhole size. A thinner and pinhole-free palladium membrane is therefore important for practical applications.

2.2.5 Different type composite palladium membranes

Palladium-based membranes can be classified into two types, self-supported dense metallic membranes and composite type membranes. Itoh and Xu [1] have studied the hydrogen flux in 100 μm Pd plate at a temperature range from 200°C to 350°C, the results are presented in Figure 6. This membrane had an infinite selectivity; however, its hydrogen permeation rate was very low. Generally, massive palladium sheets or plates are not suitable for hydrogen separation due to low hydrogen permeation flux and high costs.

In order to reduce the material cost and gain a higher hydrogen permeation rate, composite palladium membranes have been developed. This kind of palladium membranes consists of a thin selective layer deposited on porous supports. Composite palladium membranes combine high permeation flux, provided by a thin selective top layer, and a reasonable mechanical stability, which results from the underlying porous structure. There is large literature dealing with this kind of membranes. In 1988 Uemiya [11] and his co-workers used electroless plating to deposit palladium membranes ranging from 13 to 20 μm on the outside of a porous glass tube with 0.3 μm pore size. There was an infinite hydrogen selectivity, which meant a pinhole free palladium membrane was obtained. In 1990, they [12] reported a composite palladium-ceramic membrane with an 8.6 μm layer of palladium on the outside

surface of a porous alumina cylinder. The hydrogen selectivity for this membrane was not reported. In 1991, Uemiya and his coworkers [4] reported a 4.5 μm thickness palladium membrane deposited on porous glass tube with 0.3 μm pore size by electroless plating. In 2000 Itoh and his coworkers [13] reported a composite palladium membrane (electroplating 4 μm palladium on porous ceramics), with a hydrogen permeation rate almost six times higher than for the 100 μm Pd plate. The selectivity of this membrane was estimated to be higher than 10,000, which meant pinholes or cracks had existed in the palladium membrane.

Studies were also conducted with the aim of modifying the pore size in the substrates for composite palladium membranes. Collins and Way [2] deposited a 11.4 μm palladium film on a macro-porous ceramic tube support with an inner surface covered by thin multiple layers with 0.1 to 0.2 μm micro-porous membrane to modify the pore size by electroless plating. The selectivity of H_2/N_2 at 550°C was 650.

An important problem in ceramic or glass composite membranes is the structural instability resulting from the mismatch of thermal expansion coefficient between the palladium film and the nonmetallic substrate. Therefore, small differences in expansion coefficients are beneficial for membranes. This problem was addressed by Rakesh Govind and Devendra Atnoor [14] in 1991. They developed a composite palladium membrane consisting of about 5 μm palladium on porous silver disks because both metals have similar thermal expansion coefficients. Considering the cost of silver, stainless steel composite Pd-based membranes seem to be more promising for the manufacture of technical membranes due to similar thermal expansion coefficients. In addition, such membranes are easy to process and have high thermal stability, mechanical strength, corrosion resistance and low cost.

A 10.3 μm Pd, 1.6 μm Ag asymmetric membrane deposited on 316L porous

stainless steel with a pore size of 0.5 μm prepared by successively palladium and silver plating in an electroless hydrazine bath was reported by J. Shu and co-authors [15] in 1995. However, an atomic inter-diffusion layer between the thin palladium layer and the stainless steel components took place during high temperature processing. To inhibit the interface reactions between the neighboring layers, an ultrathin 0.1 μm titanium nitride intermediate barrier layer between the Pd-Ag alloy membranes and the porous stainless steel was introduced.

As commercially available sintered porous stainless steel substrates in forms of either sheets or tubes have too large pores, a relatively thick palladium membrane had to be deposited to obtain an impervious composite membrane. One of the solutions was surface modification. A shot peening surface treatment was practiced on a 0.5 μm -size piece of 316 L stainless steel by Jemaa and his co-authors [16]. As a result, modified porous stainless steel substrates with reduced surface pore sizes were obtained. For a 6 μm palladium film thickness, there was no argon permeation through this membrane at 673 K. Some of the results obtained are summarized in Figure 6. It can be seen that the hydrogen permeation flux can be increased by two ways: the reduction of the palladium thickness and the increase of operating temperatures. As the increase of temperature can affect the membrane structure in industrial applications, the main focus of future research is on obtaining a pinhole-free palladium membrane with high hydrogen permeation rate, even using at low temperatures.

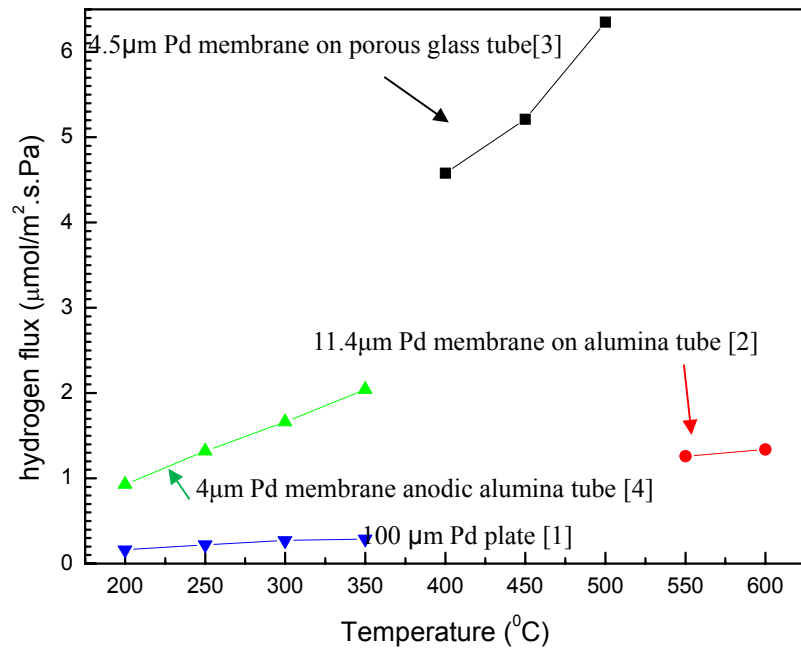


Figure 6 Hydrogen fluxes of palladium membranes as a function of temperature

2.3 Electro-deposition of aluminum in non-aqueous solution

Aluminum has many interesting characteristics, including low density, non-toxicity, good electrical and high-thermal conductivity, high-corrosion resistance, low neutron absorption, and stable mechanical properties at cryogenic temperatures. These characteristics make aluminum very useful in various industrial applications, including coating steel parts for corrosion protection in aircraft structure and cars [3], and the cladding of uranium fuel in power plants [17]. In recent years, thin aluminum films have generated much attention in the development of novel micromachining processes [4]. Anodized aluminum as a template is another attractive application of aluminum, which has been used in fabrication of nano-materials. Such templates, fabricated through a simple electrochemical process in various acidic electrolytes, have been a subject of interest due to its hexagonal pore structure, inexpensive processing and easy dissolution to free the deposited materials.

2.3.1 Tetrahydrofuran (THF) solution for electroplating aluminum

As the reduction potential of aluminum is negative, only non-aqueous inorganic, or organic electrolytes systems, or molten salts can be used for electrolytic deposition of aluminum. The low volatile and inflammable THF bath is a typical solution used in aluminum electroplating. Non-aqueous solution, however, has low conductivity, and require proper choice of electrolytes [18]. In THF bath, the colorless tetrahydrofuran (C₄H₈O) is often employed as the solvent. Two kinds of electrolytes are applied in the THF bath. AlCl₃ is the aluminum containing component, while LiAlH₄ plays an important role in enhancing the solution conductivity.

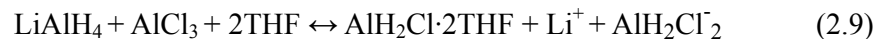
2.3.2 Reaction of the solvent and the solutes in THF

When the electrolytes AlCl₃ and LiAlH₄ are dissolved in THF bath, the following chemical reactions take place [19].

In a solution with molar excess of AlCl₃, the reaction can be expressed as



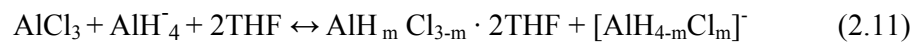
In equal molar solution, the following reaction happens



In the solution with molar excess of LiAlH₄, the following reaction can be observed



The total reaction of electrodeposited aluminum can be expressed as the Schlesinger reaction



The following equilibrium also exists when AlCl₃ dissolves in solution.



2.3.3 Species of aluminum complex ions in THF solution

The distribution of hydro-chloro-aluminate species formed in the reaction depends on the molar ratio 'r' of AlCl_3 to AlH_4^- ions (i.e. $[\text{AlCl}_3]/[\text{AlH}_4^-]$) in the solvent, and two compositional regimes may be identified as Cl^- rich, where $[\text{AlCl}_3] > [\text{AlH}_4^-]$, and conversely, H^- rich. The structures of the aluminate species that are possibly present [20] in the THF bath are shown in Figure 7.

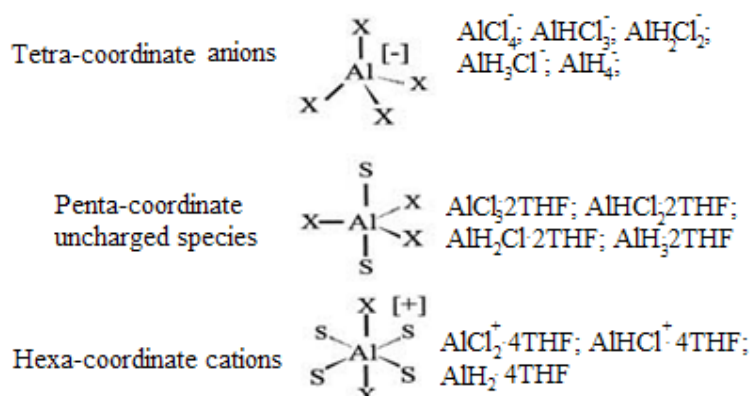


Figure 7 Structures of aluminate species possibly present in the hydride bath [23]

As discovered by Lefebvre [20] using NMR, the population of anionic and higher H^- content aluminates increased as the ratio of LiAlH_4 was increased. The Cl^- rich solutions favor uncharged aluminates of higher chloride content and lower hydride content, while H^- rich ones favor anions aluminates of higher hydride content. In H^- rich baths the higher H^- substituted aluminates are expected to become more prominent.

2.3.4 Effect of water in the solution

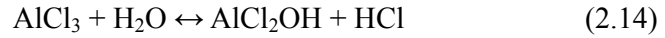
In the THF solutions, if some water is present, the hydride will have to be

reduced, accompanied by the release of hydrogen gas [21].



Small amount of water causes no significant change, but high water content leads to the deterioration of the hydride electrolyte.

AlCl_3 can also react with water by the following reactions:

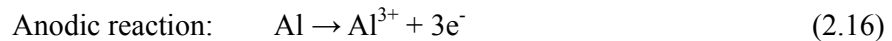


Since water-free chemicals are required in the solution, the preparation of electrolyte should be carried out in a nitrogen-filled or argon-filled gas glove box to avoid moisture and reduce contamination that results from described reaction with water.

2.3.5 Fundamental of electro-deposited aluminum in THF solution

(1) General principles

Electroplated aluminum coatings can be obtained using a non-aqueous THF solution that contains LiAlH_4 and AlCl_3 . The electrolytic reactions can be expressed as follows:

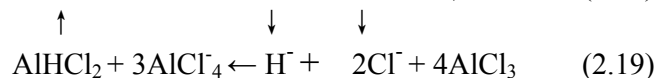
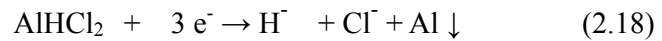


Cathodic reaction (overall electrode reaction [22]):



where AlX^- can be AlCl_4^- , AlHCl_3^- , $\text{AlH}_2\text{Cl}_2^-$, AlH_3Cl^- , AlHCl_2^- , depending on the composition of the situation.

For example, if it is AlHCl_2^- , the cathodic reaction can be expressed as:



In the solution with a molar excess of AlCl_3 over LiAlH_4 , the dominant species are AlCl_4^- and AlHCl_3^- ; whereas when there is an excess of AlH_4^- , the dominant species is AlH_3Cl^- .

The chloride and hydride anions, denoted by X^- in the overall reaction equation (2.19), are unstable and can further react with neutral molecules.



In this way, all the aluminum present in the solution in the form of anions and neutral molecules are reduced at the electrode.

(2) Mechanism of aluminum deposition

The mechanism of electro-deposition of aluminum is relatively complex since aluminum possesses three valence electrons and can exist only in one stable oxidation state. Therefore the reduction of Al^{3+} solution species necessarily implies a multi-step, multi-electron mechanism. There are various mechanisms in THF solution proposed by different authors:

(a) GÁLOVÁ's mechanism

The following mechanism from AlCl_3 — LiAlH_4 —THF electrolyte was suggested by J. Eckert and M. GÁLOVÁ in 1981 [22]:



The combined reaction is as follows:



If there is an excess of AlCl_3 in the electrolyte, the charge transfer (step1) is the rate-determining step; whereas if LiAlH_4 is in excess, the chemical reaction step 2 and step 3 determine the rate of the overall process at higher over-potential values.

(b) Badawy's mechanism

In 1987, Badawy [23] and his coworkers put forward another mechanism for AlCl_3 - LiAlH_4 /THF-toluene.



AlX_4^- may be AlHCl_3^- , $\text{AlH}_2\text{Cl}_2^-$, AlH_3 , according to the solution composition.

The primary product of the electrode process, the anions X^- , which are chlorides and hydrides, are not sufficiently stable in this medium and can react quickly with neutral molecules present in the solution to form new anionic electro-active particles.



AlX_3 represents AlH_2Cl , AlHCl_2 , or AlH_3 . In this way, the aluminum is reduced at the electrode independently, whether it was originally in the solution in the form of electro-active anions or inactive neutral molecules.

(c) Nucleation mechanism of aluminum in THF bath

The nucleation and growth mechanism was studied by M.C. Lefebvre and his coworkers [24]. It was described as a kinetically controlled, three-dimensional growth with instantaneous nucleation on glassy carbon with poor adhesion. It was a diffusion-controlled process which occurs on the gold substrate.

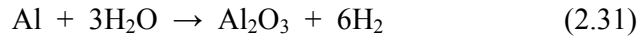
2.4 Formation of anodic aluminum oxide (AAO) template

An oxide film can be grown on certain metals such as aluminum, niobium, tantalum, titanium, tungsten, and zirconium through an electrochemical process called anodizing. Aluminum is unique among these metals due to its highly dense hexagonal pore structure. The history of electrochemical oxidation of aluminum dates back to the beginning of the nineteenth century. In recent years there has been an increasing interest in anodic aluminum oxide due to its large surface area and a relatively narrow, hexagonal pore size structure, which can be used in nano-material fabrication. The AAO membrane is an ideal template because it possesses many desirable characteristics, including tunable dimension of pores, good mechanical strength and thermal stability. The oxide layer formed by anodization provides an advantageous combination of a good conducting layer and an insulating layer, which can be successfully applied in electrical engineering and electronics [25]. In addition, alumina is easy to be dissolved to free the deposited nano-materials.

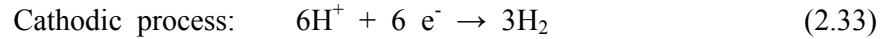
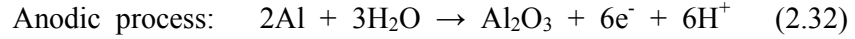
2.4.1 Electrochemical reaction in AAO

The anodizing process can be attained by establishing an electrical circuit between a cathode and the aluminum through an acidic electrolyte. During the anodization process, the aluminum piece serves as the anode of a DC power supply based on any chromic, sulfuric, phosphoric, or oxalic acid electrolyte. The cathode can be any electronic conductor that is inert in the anodizing bath. Once the circuit is closed, electrons are withdrawn from the metal at the positive terminal and allow ions at the metal surface to react with water to form the oxide layer on the aluminum surface. The electrons return to the bath at the cathode where they react with hydrogen ions to produce hydrogen gas [7]. When aluminum is anodized, aluminum oxide is

produced from the reaction, which can be summarized as follows [26]:



This represents the sum of two partial processes



2.4.2 Pore structure in anodic aluminum oxide membranes

The anodic aluminum oxide grows as a very uniform, hexagonal porous array. This type of packing is optimal, which means the porous array packs as densely as possible. During the anodization process, the anodized aluminum layer first starts forming a barrier layer. As it thickens, the pores develop, and the oxide grows as a porous membrane [7]. The barrier layer remains at the bottom of the porous membrane, and forms a “barrier” between the aluminum surface and the porous aluminum oxide. The interface of the porous array and the barrier layer forms a semi-spherical shape, as illustrated in Figure 8.

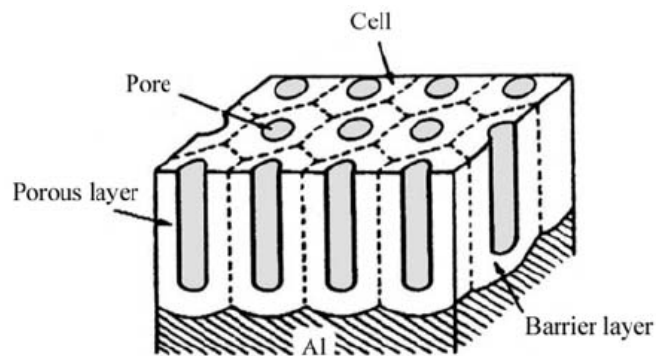


Figure 8 Schematic diagram of porous oxide film structure [7]

2.4.3 Mechanism of self-ordered pore formation

Although the electrochemical anodizing reaction has been known for a long

time, the physical mechanisms underlying this remarkable self-organization process are not well understood yet. One pore formation mechanism supported by O. Jessensky [27], Parkhutik [28], Wu [29], and Huang [30] is as follows: when an electric field is applied to aluminum during the anodizing process, there is an electrical breakdown at the beginning, and an aluminum oxide layer grows on the entire surface. Thus, surface roughness is increased by the volumetric expansion associated with the conversion of aluminum into aluminum oxide, resulting in fluctuations on the surface. This volume expansion leads to compressive stress during the oxide formation on the oxide/metal interface. The anodic oxide layer builds on the surface of aluminum and simultaneously penetrates the substrates. When the aluminum oxide mask becomes sufficiently thick, the electrical breakdown cycle stops, and a barrier type aluminum oxide is formed. This surface fluctuation causes the local electric field redistribution. During the early stage, the film on the convex parts of the surface becomes thicker than in the depressions. With a concave geometry developing, the electric field is slightly higher inside the depressions, and field-assisted dissolution promotes local oxide thinning. As reported by Q. Huang, dielectric breakdown always initiates along the local electric field direction, and electrochemical dissolution is also higher along the local maximum electric field direction. This field-enhanced dissolution starts within the formed oxide, and pores begin to nucleate. In addition to the mechanical stress at the metal-oxide interface, repulsive forces also exist among the neighboring pores, promoting the formation of a hexagonally ordered pore arrangement, while the expansion stress in the vertical direction pushes the pore wall upwards. The morphology is transformed until a steady state governs the film growth, and deep pores continuously grow as the anodization continues. The dissolution at the electrolyte/oxide interface is equilibrated with oxide growth at the metal/oxide

interface. The formed anodic oxide film consists of two regions: a thick top region of the porous oxide and a thin bottom region of the barrier oxide.

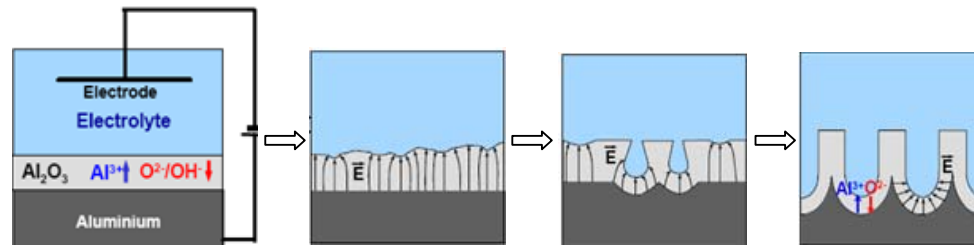


Figure 9 Schematic diagram of self-organized formation of pore structure

It has been reported that the type and concentration of the electrolyte, anodizing voltage, temperature and impurities can affect the self-organized hexagonal pore structure in the anodic alumina. Sulfuric acid, phosphoric acid and oxalic acid are the three main electrolytes in anodizing aluminum. The anodization of aluminum is carried out in sulfuric acid for low potential ranges (5~40 V), oxalic acid for medium potential ranges (30~120 V), and phosphoric acid for high potential ranges (80~200 V). A set of anodization parameters in different electrolytes are summarized in Table 1 [27].

Table 1 Anodization conditions for various electrolytes

Electrolyte	concentration(mol/l)	Temperature (°C)	Volt (V)	Diameter (nm)
Sulfuric acid	0.5	0	5~40	30
Oxalic acid	0.3	10	30~120	45
Phosphoric acid	1.0	0	80~200	400

CHAPTER 3 Fabrication of Al films by electroplating

Fabrication of anodic alumina template is closely related with the choice of aluminum substrate. In general, pure aluminum foils with different thicknesses are used [31-33]. Thin aluminum film obtained by deposition using sputtering or electroplating is another choice [34]. Sputtering deposition method has an advantage of flexible control of the coating thickness on substrate, but it is impractical because of the high cost of the process. In comparison, the use of electroplating may reduce cost, allow controlling the thickness, obtaining desirable sample size, and at the same time reducing the thermal stress in the substrate.

In recent years, there has been a considerable literature concerning electroplating aluminum in THF bath. However, most of the work is concentrated on the speciation of aluminum complex ions in THF solution [5], the nucleation and growth mechanism of aluminum deposits in THF solution [6], and the mechanisms of the reaction during the electroplating [7,8]. The characterization of the electroplating aluminum films obtained in THF solution and investigation of its effect on the later anodizing process have not been reported yet.

The aims of this chapter are to study the effects of various electrochemical conditions on the formation of deposited aluminum films. The crystalline structure of the coatings and the texture will be analyzed. The obtained Al films will be used for further fabrication of AAO template.

3.1 Experimental procedure

In order to achieve good AAO templates, homogeneous electroplated aluminum films are essential. This section will introduce the process to prepare aluminum films

using the electroplating method, and then the as-deposited aluminum films are characterized.

3.1.1 Solution preparation

The solvent tetrahydrofuran (THF), purchased from Fisher Scientific, was used as received. The anhydrous aluminum chloride (AlCl_3 concentration 99%) in the form of a yellowish powder is a commercial product obtained from Alfa Aesar. White lithium aluminum hydride powder (97%) was also supplied by the same company.

As mentioned in the literature review, water reacts with the solution; consequently, the preparations of all the solution were carried out in a glove box, avoiding the access of air and humidity. In order to eliminate the traces of oxygen or water in the atmosphere gas, nitrogen was introduced into this closed system for half an hour before the solutes were mixed with solvent.

In order to study the effect of concentration of aluminum chloride and lithium aluminum hydride on microstructures of deposited aluminum films, two groups of solutions were prepared. The first group was composed of solutions with a constant aluminum chloride concentration, but with different concentrations of lithium aluminum hydride. The second group consisted of solutions with a constant lithium aluminum hydride concentration, but with different concentrations of aluminum chloride. The solutions were prepared in the following manner: firstly, the AlCl_3 powder was added in small amounts to the THF solution. Because temperature increases during the process, the solution was left to cool for half an hour. Then the LiAlH_4 powder was dissolved into this solution. As the THF solution vaporizes during the solution preparation process, the solution concentration was calculated by weighing the THF solution, and this weight was converted into volume of the THF. The density used for calculating the THF volume is 0.888 g/ml. The concentrations of

prepared solutions are present in Table 2 and Table 3.

Table 2 Solution Preparation with constant AlCl_3 concentration

No	M (AlCl_3) / mol/l	M(LiAlH_4)/ mol/l	(Al total)/ mol/l	Ratio (AlCl_3 : LiAlH_4)
1	0.58	0.19	0.77	3:1
2	0.58	0.29	0.87	2:1
3	0.58	0.15	0.73	4:1

Table 3 Solution Preparation with constant LiAlH_4 concentration

No	M (AlCl_3) / mol/l	M(LiAlH_4)/ mol/l	(Al total)/ mol/l	Ratio (AlCl_3 : LiAlH_4)
4	0.94	0.30	1.24	3:1
5	0.60	0.30	0.90	2:1
6	1.18	0.30	1.48	4:1

3.1.2 Electro-deposition of aluminum films

The electrochemical experiments were done in a conventional three-electrode cell, where an aluminum plate (15×50×3 mm) was used as a counter electrode in order to compensate for the loss of aluminum ions in the solution during the electroplating process. A piece of stainless steel metal with dimensions of 15×50×1.5 mm was employed as the working electrode, and a saturated calomel electrode (SCE) as a reference electrode, to which all potentials in this chapter are referred. Before electroplating, the cathode (stainless steel substrate) was first washed with acetone in ultrasonic bath for 15 minutes to get rid of any existing grease, then flushed with distilled water and dried with a hand dryer. All the experiments were done in a wide range of potentials, from -2 V to -6 V at a -0.5 V interval, measured vs. SCE with the duration time of 10 minutes in all prepared solutions. All the deposition of aluminum was carried out by a computer-controlled Auto-lab PGSTAT30 Potentiostat.

3.1.3 Characterization method of as-deposited aluminum films

The covering power is a primary factor for obtaining a homogeneous aluminum

films. The covering power and microstructures were investigated with a scanning electron microscopy (SEM), employing a Philips XL30 field-emission-gun system. All the samples were cut and mounted in order to observe the thickness of the as-deposited aluminum films.

In order to observe the crystalline structure and phase composition, X-ray diffraction (XRD) was used. The XRD was carried out on a rotating anode Rigaku X-ray generator with Cu K α ($\lambda = 1.540562 \text{ \AA}$) using an accelerating voltage of 40 KV and a current of 40 mA. In order to distinguish the overlapping peaks from the substrate, two experiments were performed. One was a normal θ - 2θ scan and the other was a grazing angle of 1.5° scan.

In addition, the influence of anodizing process on texture of electroplated aluminum films was investigated. The textures of the two samples with different microstructures were determined by a Siemens D 500 diffractometer. By comparing the results obtained from the two XRD measurements, the three strongest aluminum peaks, (111), (200) and (220), were selected for aluminum texture measurement. The diffractometer was operated with a Mo K α target. The pole figures were measured using the reflection technique with 5° polar and angular intervals. The results were analyzed by TexTools software.

3.2 Optimization of the fabrication process in electroplating aluminum films

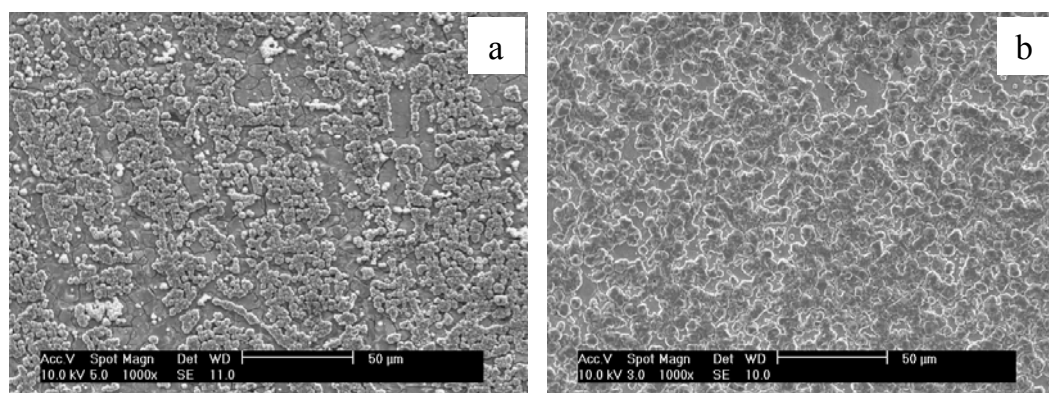
3.2.1 Factors affecting covering power

A homogeneous aluminum film is important in template fabrication and this homogeneity can be expressed by covering power. The covering power refers to the fraction of substrate that is completely covered with aluminum deposits. Various factors, such as the bath composition, the nature of the cathode surface and the surface

finish, have influence on the covering power.

Figures 10, 11 and 12 show the SEM images of as-deposited aluminum films which are obtained at increased AlCl_3 concentration (at constant LiAlH_4 concentration). At low potential $E = -2.0$ V, the covering power is low and the aluminum deposits cannot completely cover the substrate even after 10 minutes deposition. However, the covering power increases with increase of AlCl_3 concentration and applied potential. The potential required to completely cover the surface of substrate decreases when the AlCl_3 concentration increases.

When the AlCl_3 concentration is kept constant, the increase of LiAlH_4 concentration does not have significant effect on the covering power, as shown in Figures 13, 14 and 15. Also, the covering power is low at low potential ($E = -2.0$ V). However, it was found that LiAlH_4 concentration is an important factor affecting the particle size of the deposited aluminum. The lower LiAlH_4 concentration produces smaller particle size. To characterize the covering power, descriptive terms, such as dotted, cluster dotted, sparse, medium, dense and total are used. The results are summarized in Table 4.



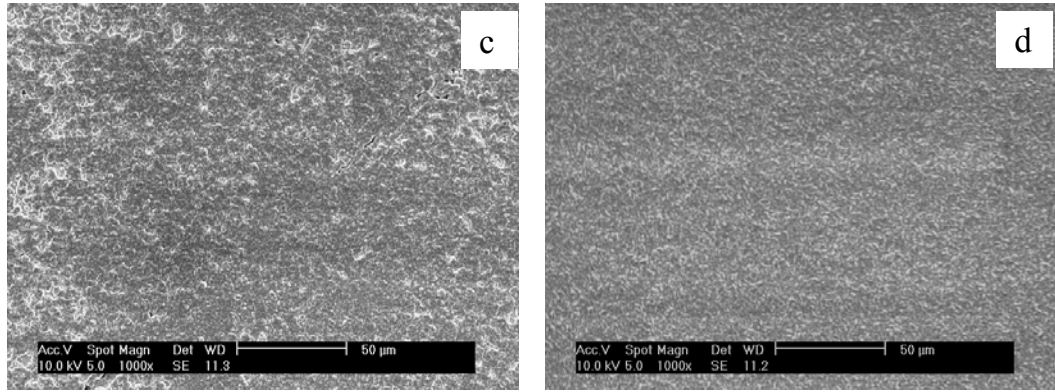


Figure 10 SEM images of as-deposited Al obtained in solution $\text{AlCl}_3 = 0.60 \text{ mol/l}$ (at constant $\text{LiAlH}_4 = 0.30 \text{ mol/l}$); $E = -2 \text{ V}$ (a), -2.5 V (b), -3.0 V (c), -3.5 V (d).

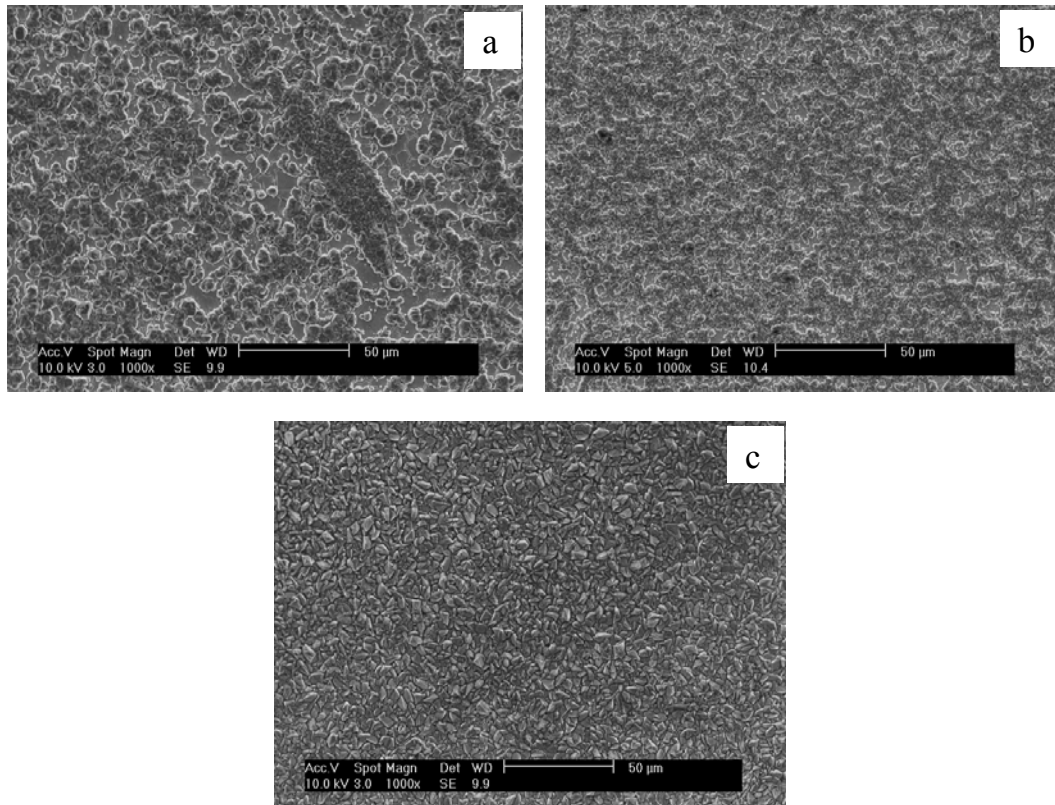


Figure 11 SEM images of as-deposited Al obtained in solution $\text{AlCl}_3 = 0.94 \text{ mol/l}$, (at constant $\text{LiAlH}_4 = 0.30 \text{ mol/l}$); $E = -2 \text{ V}$ (a), -2.5 V (b), -3.0 V (c).

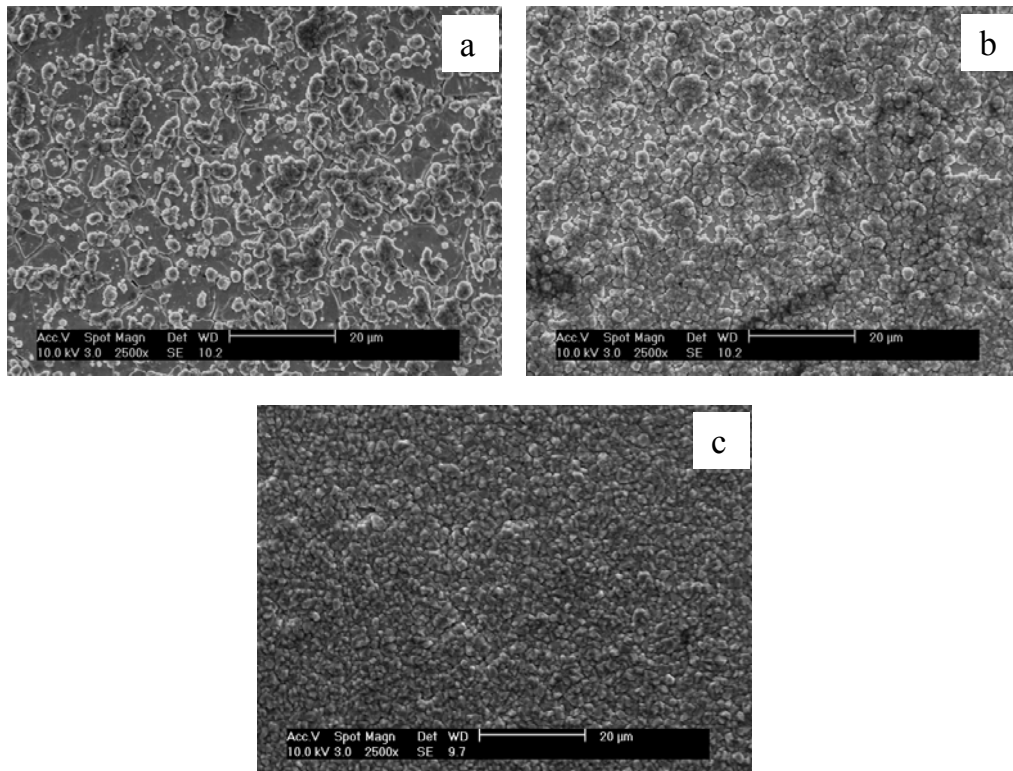
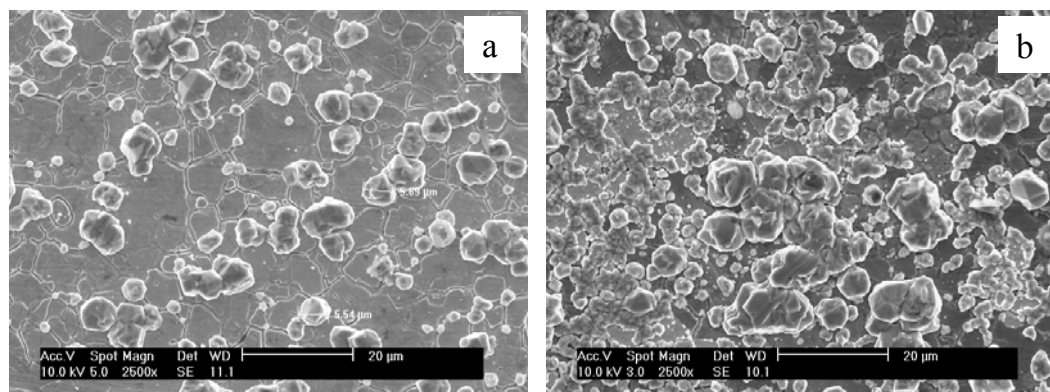


Figure 12 SEM images of as-deposited Al obtained in solution $\text{AlCl}_3 = 1.18$ mol/l, (at constant $\text{LiAlH}_4 = 0.30$ mol/l); $E = -2$ V (a), -2.5 V (b), -3.0 V (c).



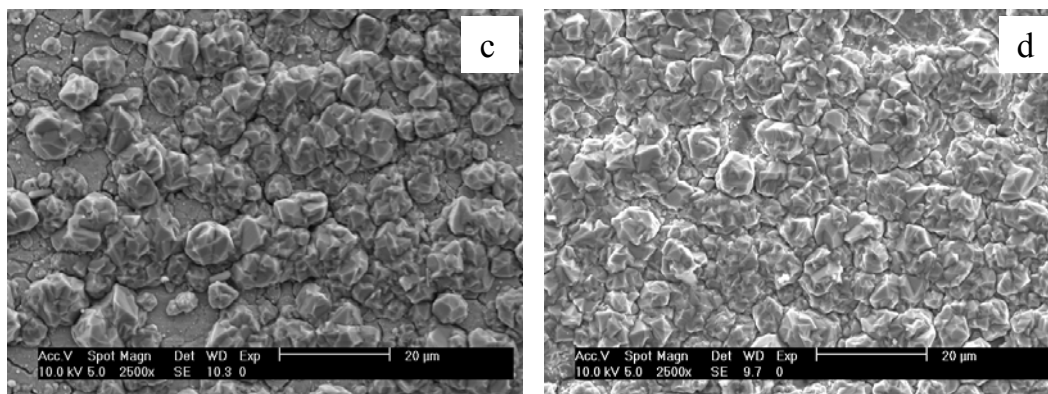


Figure 13 SEM images of as-deposited Al obtained in solution $\text{LiAlH}_4 = 0.29 \text{ mol/l}$, (at constant $\text{AlCl}_3 = 0.58 \text{ mol/l}$); $E = -2 \text{ V}$ (a), -2.5 V (b), -3.0 V (c), -3.5 V (d).

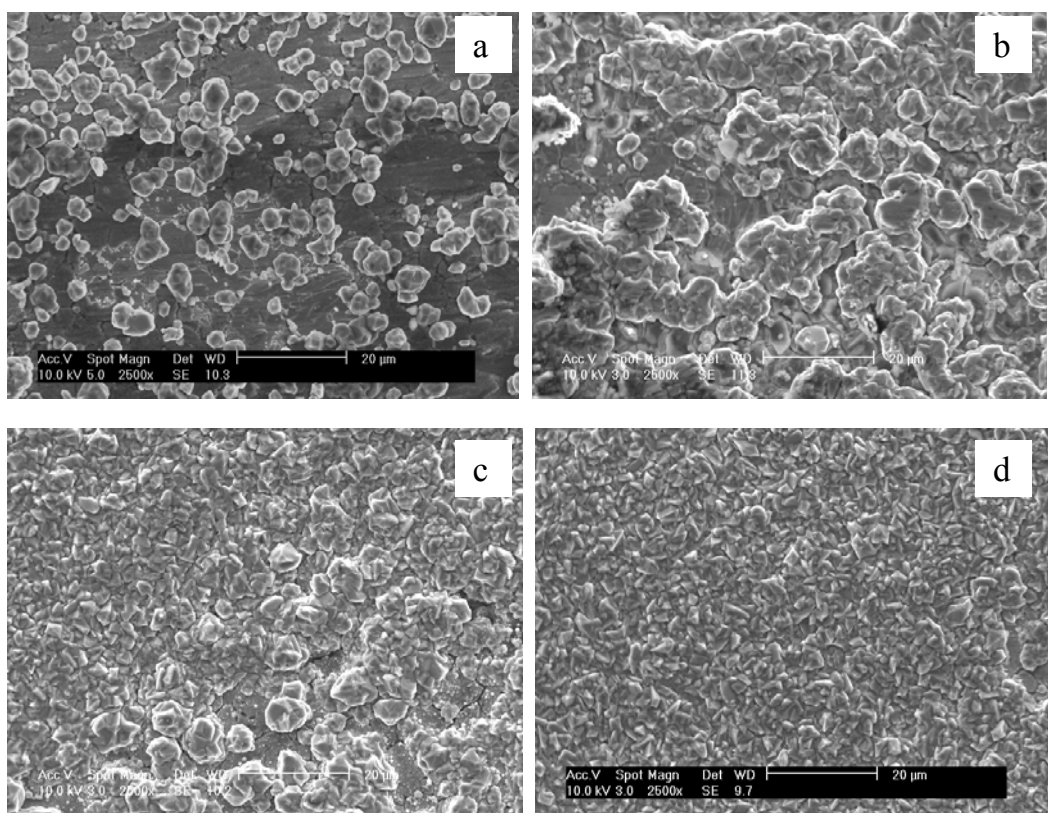


Figure 14 SEM images of as-deposited Al obtained in solution $\text{LiAlH}_4 = 0.19 \text{ mol/l}$, (at constant $\text{AlCl}_3 = 0.58 \text{ mol/l}$); $E = -2 \text{ V}$ (a), -2.5 V (b), -3.0 V (c), -3.5 V (d).

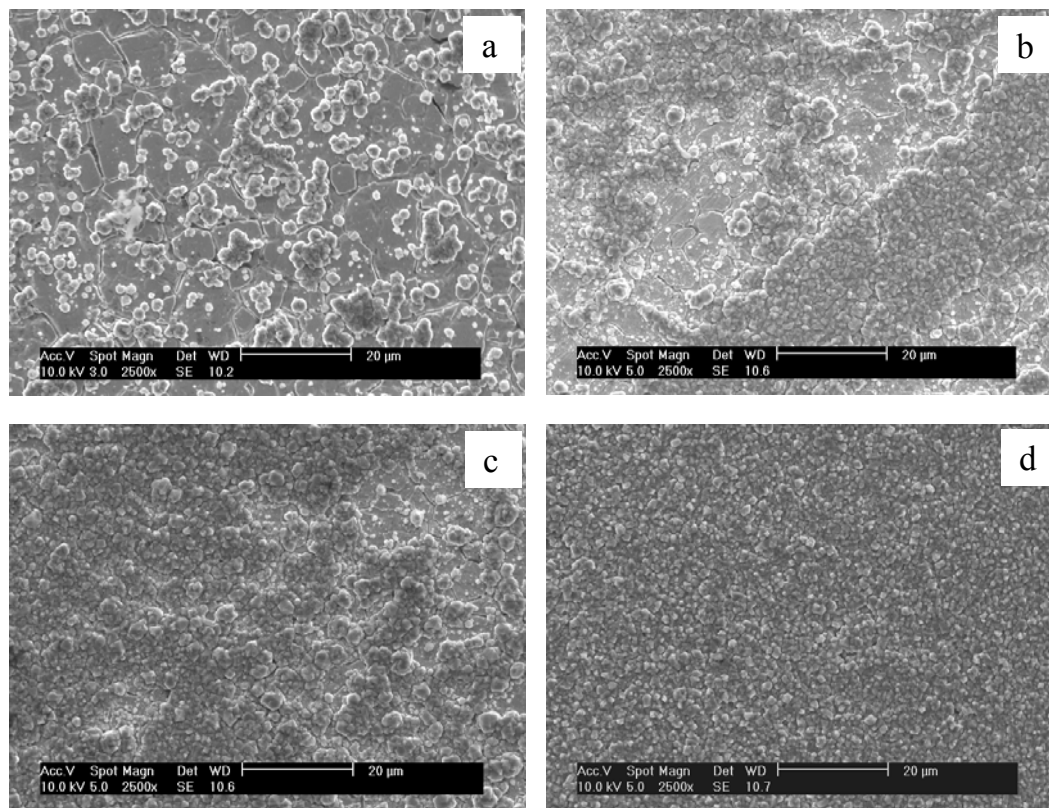


Figure 15 SEM images of as-deposited Al obtained in solution $\text{LiAlH}_4 = 0.15\text{mol/l}$, (at constant $\text{AlCl}_3 = 0.58\text{ mol/l}$); $E = -2\text{ V}$ (a), -2.5 V (b), -3.0 V (c), -3.5 V (d).

Table 4 Summary of the covering power at different electroplating conditions

Solution Potential	0.30mol/l $\text{LiAlH}_4 + \text{AlCl}_3$ (mol/l)			LiAlH_4 (mol/l) + 0.58 AlCl_3 (mol/l)		
	0.60 (2:1)	0.94 (3:1)	1.18 (4:1)	0.29 (2:1)	0.19 (3:1)	0.15 (4:1)
-2.0 V	sparse	medium	medium	Clus. dotted	Clus. dotted	dotted
-2.5 V	medium	dense	dense	sparse	sparse	sparse
-3.0 V	dense	total	total	medium	medium	medium
-3.5 V	total	-----	-----	total	total	total

Table 4 illustrates the results of the covering power of aluminum deposits on the substrate. It can be seen that the covering power changes with AlCl_3 concentration. When the AlCl_3 concentration increases from 0.60 mol/l to 1.18 mol/l, the potential required to completely cover the substrate decreases from -3.5 V to -3.0 V. When the

concentration of LiAlH_4 is changed, the covering power shows no dramatic change. However, with the decreasing of LiAlH_4 concentration, the particles become smaller, as is shown in Figures 13 to 15. With the same ratio of 3:1 of AlCl_3 to LiAlH_4 , the applied potential required decreases from -3.5 V to -3.0 V with an increase in concentration of AlCl_3 .

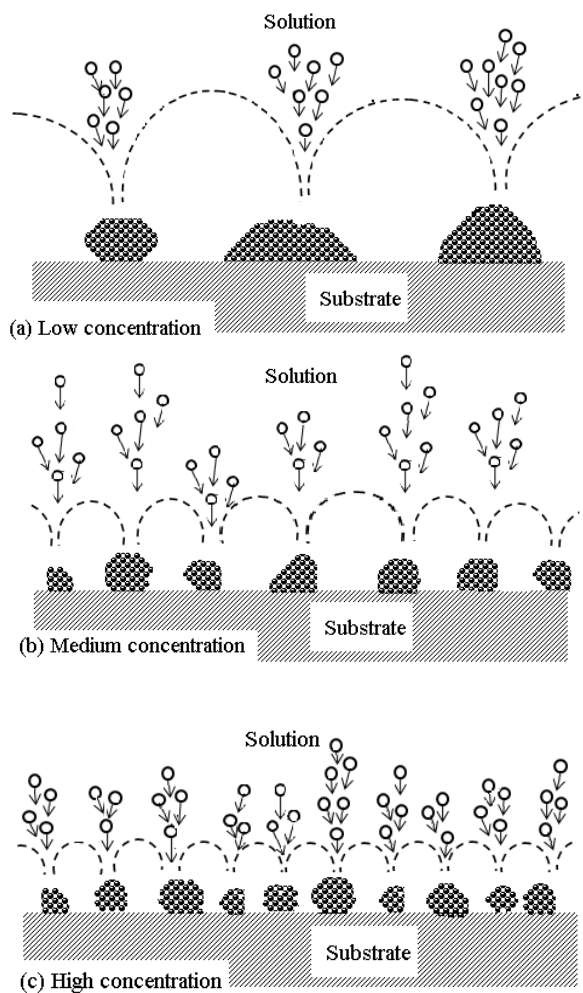


Figure16 Schematic graph of the influence of AlCl_3 concentration on covering power

As reported by Badawy [9], in non-aqueous THF solutions, the conductivity of the solution increases either by increasing the molar ratio of LiAlH_4 to AlCl_3 or by increasing the total concentration of aluminum in the solution. This increase of

conductivity with increasing concentration of LiAlH_4 is attributed to the formation of both AlHCl_2 and AlH_2Cl which generate the ionic species AlCl_2^+ , $\text{AlH}_2\text{Cl}_2^-$, and AlH_2^+ . These ionic species are directly responsible for an increase of conductivity of the solution. At a constant molar ratio of LiAlH_4 to AlCl_3 any increase in the total concentration of aluminum may also lead to an increase in the concentration of the ionic species and consequently increase in the conductivity of the solution. This means that both the increases of LiAlH_4 concentration and the total aluminum concentration may generate more species migrating towards the working electrode at the same time. The resultant higher speed-up of migration will accelerate the growth of nuclei at the surface, thus producing larger particle size. As AlCl_3 is the aluminum component, any increase of AlCl_3 concentration may also lead to an increase of nucleation rate, as explained in Figure 16. As more nucleation sites are produced on the substrate, this would undoubtedly result in an increase in covering power.

3.2.2 Factors affecting microstructure of as-deposited aluminum films

3.2.2.1 Influences of solution concentration and potential on surface morphology

In process of the aluminum film fabrication, various microstructures were obtained. Figure 17 shows the SEM images of microstructure obtained by electroplating aluminum in the THF solutions. It can be seen that the deposited aluminum particles are of different morphologies under different conditions. They may be divided into different classifications, such as (a) tetrahedron, (b) cone, (c) dendrite, (d) cedar, (e) rhombic, (f) oval and (g) semi-sphere particles. This illustrates that the microstructure of the deposited aluminum films changes with the applied potential and the solution concentration. These observations are summarized in Table 5.

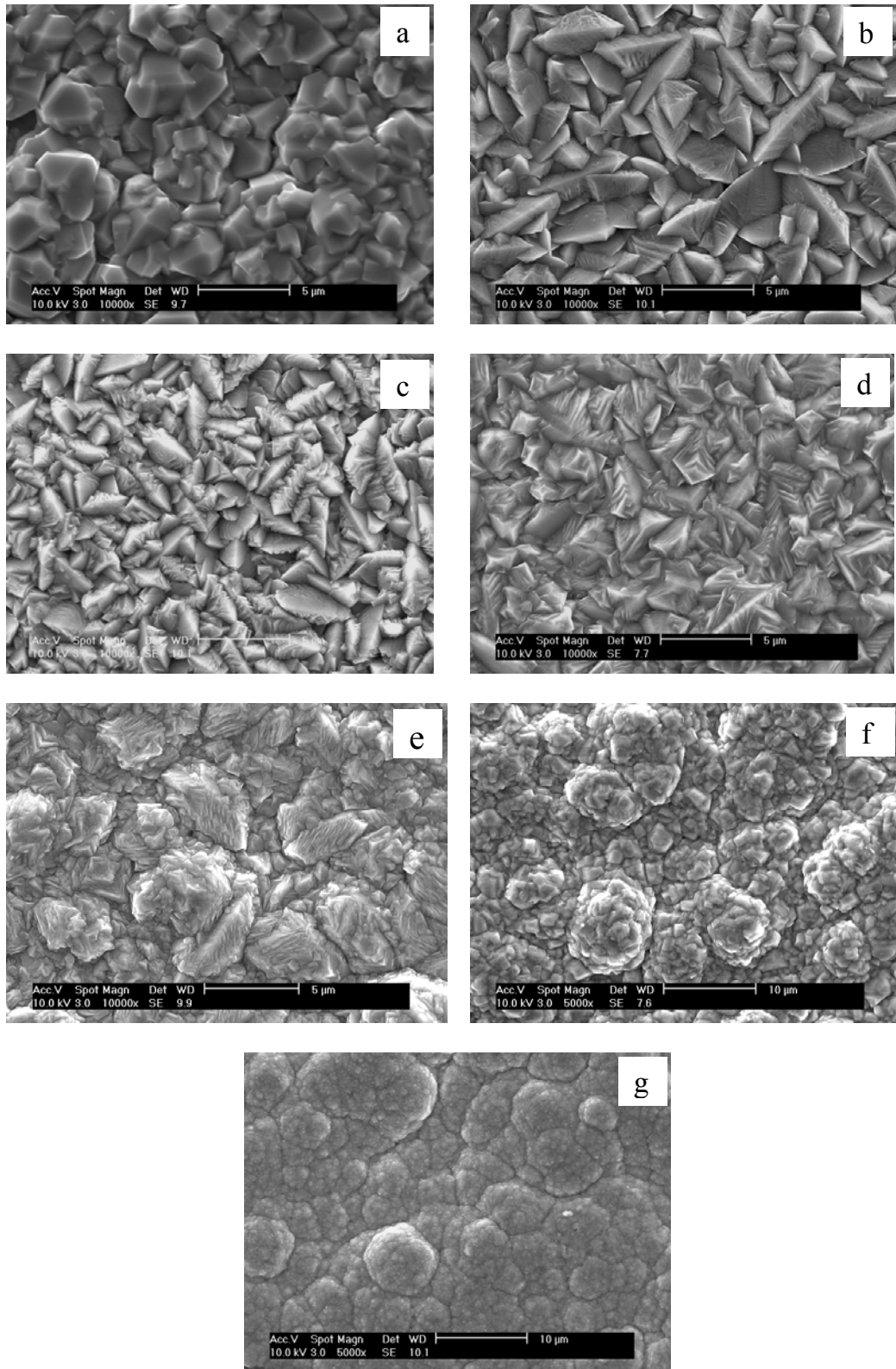


Figure 17 Microstructures obtained from as-deposited aluminum coatings

With increasing applied potential, the surface microstructure changed from large, irregular and tetrahedral particles to fine, round wavier and smooth particles. In addition, when the microstructure changed from the tetrahedral shape particles to semi-spherical particles, some fine particles produced in cluster. Under certain deposition conditions, different microstructures can be obtained within a sample. The tetrahedron grain microstructure was observed in the central area, while at the edge area other microstructures were present. In solution with molar ratio of AlCl_3 to LiAlH_4 2:1 (total concentration 0.9 mol/l), there is no coating obtained at high potential (-6 V), indicating that too low AlCl_3 concentration is ineffective in aluminum electroplating.

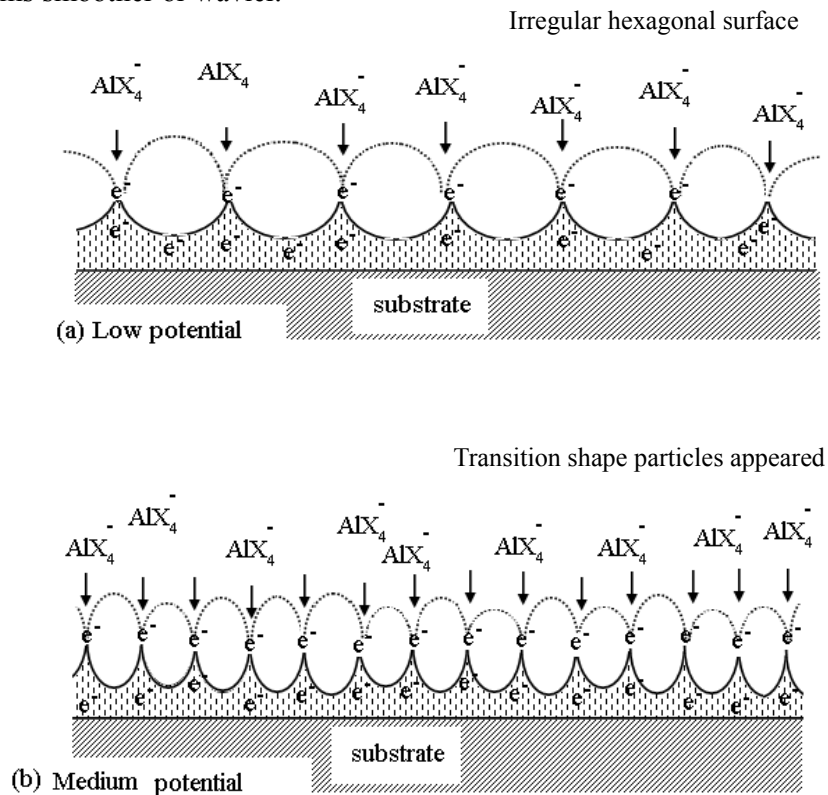
Table 5 Microstructure of as-deposited aluminum films in different concentrations under different potentials (Notation is illustrated in Figure17)

Solution potential	LiAlH ₄ (mol/l) + 0.58 AlCl ₃ (mol/l)			0.30mol/l LiAlH ₄ + AlCl ₃ (mol/l)		
	0.29 (2:1)	0.19 (3:1)	0.15 (4:1)	0.60 (2:1)	0.94 (3:1)	1.18 (4:1)
- 3.5 V	a	a+b	a	a+b+c	a+b+c	a+b
- 4.0 V	a+b	a+b+c	a+b	a+b+c	a+b+c	a+b+c
- 4.5 V	a+b+c	a+b+c+d	a+b	a+b+c+d	a+b+c+d	a+b+c+d
- 5.0 V	a+b+c+d	a+b+c+d	a+b	a+b+c+d	a+b+c+d	a→f
- 5.5 V	a+b+c+d	a+b+c+d	a+b	g	a→f	a→g
- 6.0 V	-----	a+b+c+d	a+b+c	-----	a→g	a→g

It can be seen (Table 5) that the higher the applied potential, the more complex the microstructure. The similar phenomena were observed in the change in concentration. The higher concentration also produces more complex microstructures both in the solutions with 0.94 mol/l and 1.18 mol/l AlCl_3 .

One mechanism, proposed by Watanabe [10], may explain the development of aluminum microstructures in electroplated films. As depicted in Figure 18, the number

of aluminum ions discharge events per unit area or per unit time is smaller at lower potential. However, even at low potential, these ion discharge event will still occur preferentially at protrusion. Once this nucleation occurs at these protrusion sites, they will grow, producing aluminum films with high surface irregularities, as shown in Figure 18. However, the higher solution concentration produces higher densities of aluminum metal ions and higher applied potential can accelerate the migration of metal ions to substrate. When these metal ions are discharged on the surface of the cathode, i.e. the substrate, the similarly charged aluminum complex species repel each other if they are brought closer than a critical distance from each other. This will redistribute the aluminum ions on the surface. Thus, higher potential and higher concentration will result in a redistribution of adatoms over the substrate surface, allowing the discharge sites to be more uniformly distributed, making the surface of plated films smoother or wavier.



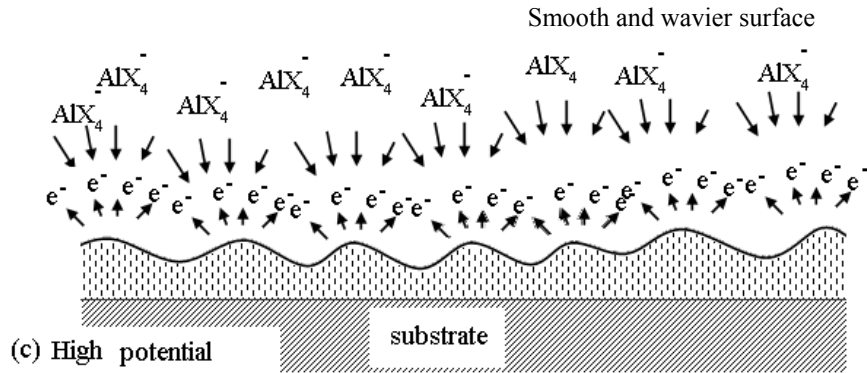


Figure18 Schematic illustration of the mechanism of formation of different microstructures

In the present deposition system, the current density distribution varies at the cathode surface. Usually the edge area has a higher current density; while the middle part has a lower current density. When the aluminum adatoms redistribute, the edge area still has higher current density than the central area, which results in microstructural difference between these areas.

3.2.2.2 Influences of solution concentration and potential on thickness

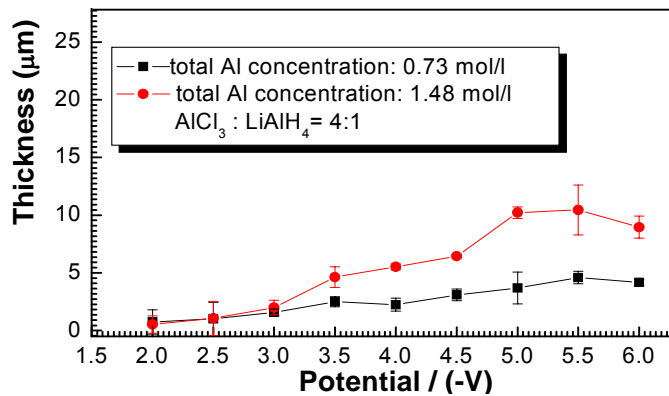


Figure 19 Coating thickness vs. potential obtained with $\text{AlCl}_3:\text{LiAlH}_4 = 4:1$

Figure 19 shows the variation of thickness in electroplated aluminum film with applied potential after deposition time of 10 minutes. The electroplating solution was

AlCl_3 and LiAlH_4 solutes dissolved in THF solvent, with the ratio AlCl_3 to LiAlH_4 , 4:1. Two different solution concentrations, 0.73 mol/l and 1.48 mol/l were studied respectively.

As illustrated in Figure 19, the film thickness increases with an increase of the aluminum concentration from 0.73 mol/l to 1.48 mol/l around electroplating potential of -3 V. However, at low applied potential, this trend is not obvious. This might be due to the fact that the covering power of the deposited aluminum is very low at low potential; below -3 volts the surface of the sample is not completely covered with aluminum deposits. This low covering power has already been confirmed by the SEM images. Starting from -3 V potential, the thickness gradually increases. However, there is a slight drop after -5.5 V. This drop can be explained because aluminum is mainly supplied by AlCl_3 , while the solution conductivity is mainly determined by LiAlH_4 . At higher applied potential, the deposition rate is higher. In a Cl^- rich solution, (AlCl_3 : $\text{LiAlH}_4 = 4:1 > 3:1$), the lack of lithium aluminum hydride may lead to a decrease in conductivity of the solution at higher deposition rates; and thus might cause the decline of the total aluminum ions reaching the surface. A decrease in the observed electroplating films thickness may result from this process.

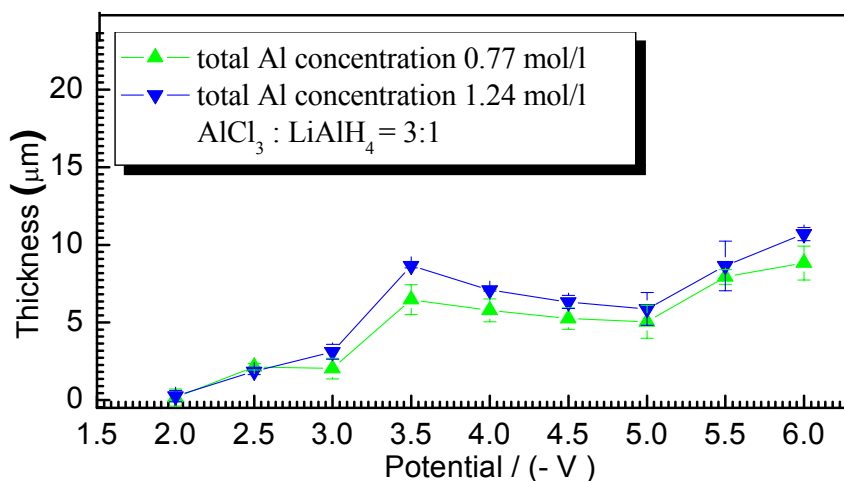


Figure 20 Coating thickness vs. potential obtained with AlCl_3 : $\text{LiAlH}_4 = 3:1$

The relationship between the film thickness and potential obtained under the previously described conditions (except that the mole ratio of AlCl_3 to LiAlH_4 is 3:1 in total aluminum concentrations of 0.77 mol/l and 1.24 mol/l) is depicted in Figure 20. A similar trend as for 0.77 mol/l was observed in these solutions, e.g. the higher concentration solution produces the thicker aluminum films in both solutions. An increase in AlCl_3 can essentially increase the film thickness, as more aluminum ions are deposited on sample surfaces. A peak around -3.5 V is observed, indicating that at this potential more aluminum ions are deposited. When the potential increased to -5.0 V, there is further increase in film thickness with potential.

As investigated by Lefebvre [5], the species of aluminum complex ions in THF solution are concentration dependent. The reduction of Al^{3+} solution species is a multi-step and multi-electron mechanism. When the potential increases above -5.0 V, the energy might be so high enough to discharge more different species at the cathode surface, resulting in a further increase of the film thickness.

3.3.3 Crystalline structure of as-deposited films

For the as-deposited aluminum film, obtained using AlCl_3 to LiAlH_4 ratio of 3:1 (aluminum total concentration of 1.24 mol/l), XRD patterns (normal θ - 2θ scan and grazing angle scan with 1.5°) are shown in Figures 21 and 22. In Figure 21, XRD peaks are in the positions of $2\theta = 38.4^\circ, 43.7^\circ, 44.8^\circ, 50.6^\circ, 65.2^\circ, 78.3^\circ, 82.5^\circ, 99.5^\circ, 112.2^\circ$ and 116.6° . Comparing these peaks with those in Figure 22, it is clearly seen that the peaks occurring at 2θ values of 43.7° and 50.8° are from the stainless steel substrate. Except of these two peaks, the other peaks are in good agreement with aluminum PDF card, corresponding to crystal planes of aluminum: (111), (200), (220), (311), (222), (400), (311) and (420), respectively.

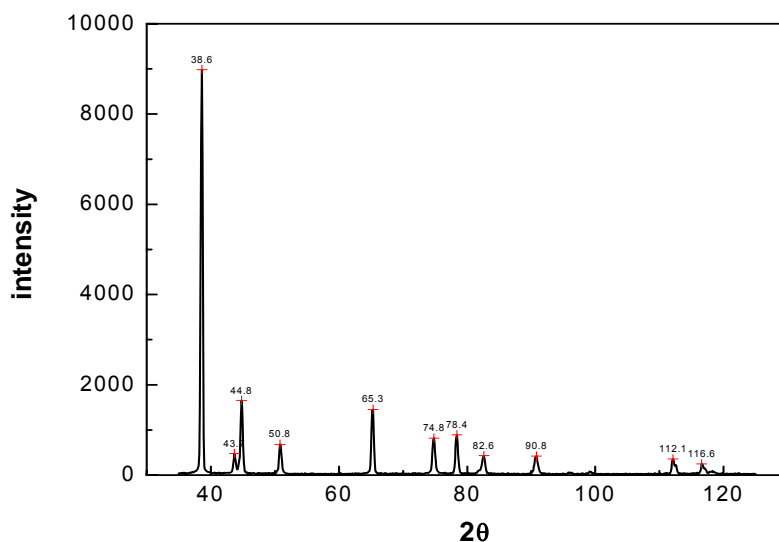


Figure 21 XRD pattern obtained on as-deposited Al coating from normal scan (AlCl_3 : LiAlH_4 = 3:1 in Al total concentration 1.24 mol/l)

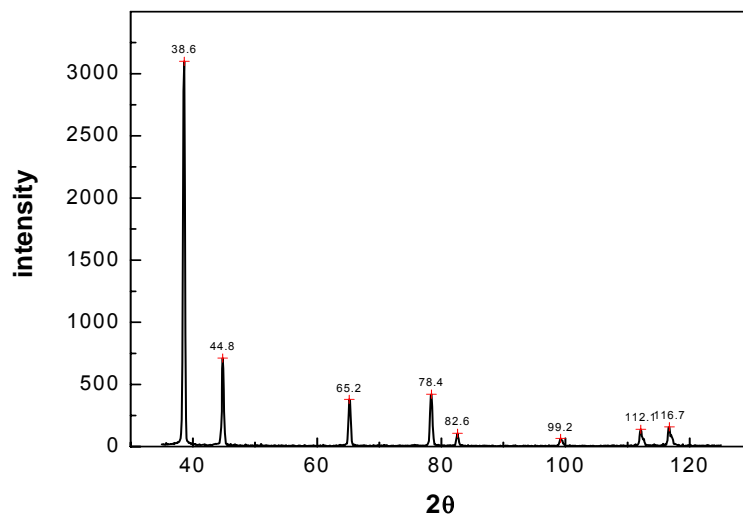


Figure 22 XRD pattern obtained on as-deposited Al coating obtained from grazing angle at 1.5° (AlCl_3 : LiAlH_4 = 3:1 in Al total concentration 1.24 mol/l)

In order to study the relationship between the surface morphology and the crystalline structure, another sample with AlCl_3 : LiAlH_4 ratio of 4:1 in solution 1.48mol/l was used for measurement. The XRD patterns obtained for this sample were shown in Figure 23. The results show that no difference between the two samples. The preparation conditions do not have any effects on the

crystalline structure.

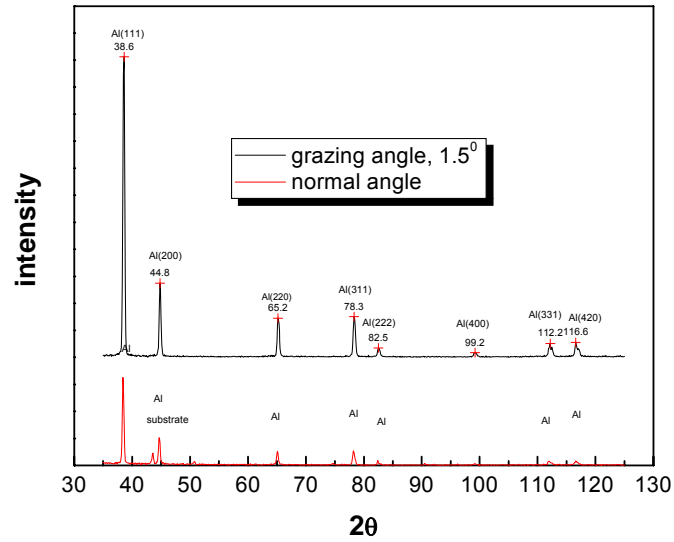


Figure 23 XRD patterns of aluminum coating obtained in solution $\text{AlCl}_3:\text{LiAlH}_4 = 4:1$ in total Al concentration 1.48 mol/l under normal and grazing angle mode.

3.3.4 Texture of as-deposited films

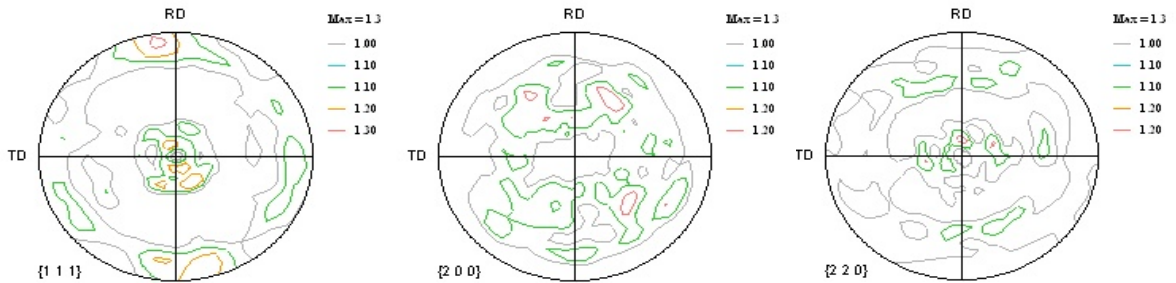


Figure 24 Pole figures (111), (200), (220) of as-deposited aluminum coating with $\text{AlCl}_3:\text{LiAlH}_4 = 3:1$ in total Al concentration of 1.24 mol/l

The three strongest diffraction peaks (111), (200), and (220) of aluminum, were chosen for texture measurements. The pole figures were measured using the reflection technique with 5° polar and angular intervals. The Orientation Distribution Functions (ODFs) were calculated using TexTool's software. The pole figures are shown in Figures 24 and 25, for samples with $\text{AlCl}_3:\text{LiAlH}_4 = 3:1$

in total aluminum concentration of 1.24 mol/l, and $\text{AlCl}_3:\text{LiAlH}_4 = 4:1$ in total aluminum concentration of 1.48 mol/l. It is seen that the strongest line is 1.3 for the coating obtained in $\text{AlCl}_3:\text{LiAlH}_4 = 3:1$ in (111) pole figure. This means that the as-deposited aluminum films only have weak texture.

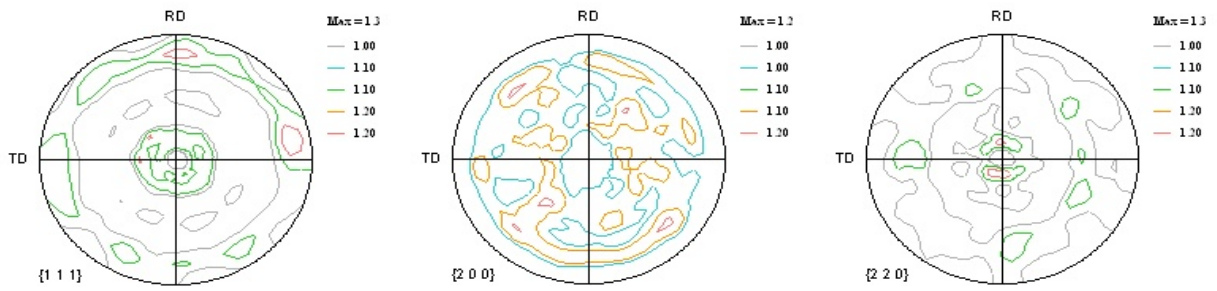


Figure 25 Pole figures (111), (200), (220) of as-deposited aluminum coating with $\text{AlCl}_3:\text{LiAlH}_4 = 4:1$ in total Al concentration of 1.48 mol/l

As described by Watanabe [10], the texture depends not only on potential, but also on the type of anions, plating temperatures, and film thickness. In general, the surface energy varies with the type of crystallographic planes. The plane with the lowest surface energy generally becomes the final growth facet seen on the top surface of the film. For fcc aluminum crystal structure, the surface energy decreases in the order of $(110) > (100) > (111)$. This might be the reason why (111) texture may be observed in as-deposited film.

3.3 Summary

In this chapter, the effects of electroplating conditions on the fabrication of aluminum films were studied. At first, six groups of solution with different ratios of AlCl_3 to LiAlH_4 (2:1, 3:1 and 4:1) and applied potentials (in the range from -2 V to -6 V) were chosen. Results show that electroplated aluminum films cannot be prepared

under high applied potential and low ratio of AlCl_3 to LiAlH_4 (2:1). The optimum experimental for the preparation of homogeneous electroplated aluminum films are in the applied potential range from -3 V to -4 V and the solution range from 3:1 to 4:1. The as-prepared polycrystalline aluminum film has a very weak (111) texture.

CHAPTER 4 Fabrication of AAO template

Anodic aluminum oxide can be used for corrosion protection, as dielectric materials in microelectronics applications [35], electronic, magnetic [36,37] and optical devices [38,39], industry filters [40,41], and bio-devices [42]. It can also be used as templates in fabricating nano-scale materials [43,44]. In this chapter, we will study the possibility that deposited aluminum films are used for the preparation of AAO templates.

There is extensive literature on fabrication of AAO templates on aluminum foils. However, for the anodic alumina obtained by anodizing electrodeposited aluminum, no study has been conducted. For comparison and better understanding of anodization process, the anodization of commercial available aluminum foil is also studied. The main purposes of this chapter are to study the influence of electrochemical conditions on the formation and morphology of AAO templates obtained by as-deposited aluminum and to prepare AAO templates for further fabrication of nano-structured palladium membranes.

4.1 Experimental procedure

Anodization of as-deposited aluminum films is the second step for the fabrication of nano-structured palladium membranes. Effects of the anodization behavior of electroplated aluminum, the microstructure and the etching time on the formation of AAO template were studied so that we can obtain optimum preparation condition. At the same time, in order to in depth understand the formation process in AAO template, some anodization experiments were done using aluminum foils.

4.1.1 AAO template fabricated on aluminum foils

In order to obtain the optimal conditions to guide the anodization of as-deposited aluminum films, three groups of experiments were first done on aluminum foils. The aluminum foil was purchased from Alfa Aesar, with a purity of 99% and 0.025 mm in thickness. All the samples were cut into 30×15 mm pieces, cleaned using acetone solution with a piece of cotton, gently rinsed with distilled water, and finally dried with a hand dryer.

The experiments in first group were performed with varying anodizing time at a constant potential of 35 V in 0.3 M oxalic acid solution to study the effect of the anodizing time on oxide morphology. The other experiments were carried out in 0.3 M (group 2) and 0.6 M (group 3) oxalic acid solution with changing anodizing voltage from 30 V to 55 V at 5 V interval at room temperature, employing the electrochemical cell shown in Figure 26.

This cell contains a 1 cm diameter opening where the aluminum foil was placed for anodization using a DC voltage source. A rubber o-ring made the opening watertight to prevent the electrolyte from leaking. A long conductive plate was placed on the back of aluminum foil in order to connect to the alligator clip at the positive terminal. A spiral platinum wire was used as a cathode.

After anodization, the remaining aluminum on the back of the anodized samples was removed using a tin (IV) chloride anhydrous solution supplied by Fisher, and then oxide specimen were rinsed with water and dried. The morphology and the thickness of the cross section were observed using a Philips XL30 FEG-SEM. Effects of concentration and applied voltage on anodizing rate were determined.

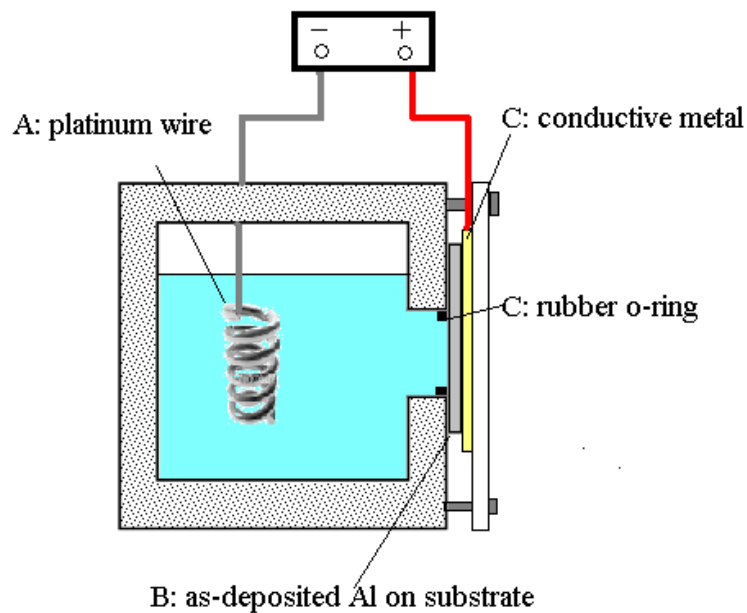


Figure 26 Schematic illustration of anodizing device

There is an oxide barrier layer inside nano-pore in as-prepared of AAO templates. The pore bottom opening is a crucial stage for the subsequent electro-deposition of palladium into pores. In order to obtain optimum experimental conditions for pore bottom opening, aluminum foil is used for this study. All the templates were obtained at a potential of 35 V with two hours anodizing time in 0.3 M oxalic acid solution. The remaining aluminum was removed in the tin (IV) chloride solution. The samples were then placed into the 5 wt. % H_3PO_4 for 15 to 75 minutes at an interval of 15 minutes in order to remove the barrier bottom layer. For comparison, the morphology of a non etching sample was also observed by SEM.

4.1.2 AAO template fabricated on as-deposited aluminum films

In order to understand the process of anodization of as-deposited aluminum films, the electrochemical investigations were performed. A conventional three-electrode electrochemical cell was used. Three as-deposited aluminum samples with the thickness of 6 μm , 9 μm and 15 μm were anodized at 30 V in 0.3 M oxalic acid. In the

process of anodization, the as-deposited aluminum film was used as the anode, while a spiral platinum wire was used as a cathode and saturated calomel electrode (SCE) as a reference electrode. All the samples were contacted with a piece of metal and then pressed against the rubber o-ring, leaving 0.8 cm^2 exposed to the electrolyte. The experiments were carried out by computer-controlled Auto-lab PGSTAT 30 Potentiostat at room temperature. When bubbles started to emerge from the aluminum samples and became progressively intensive, or the anodizing current density abruptly increased, the anodization voltage was switched off.

In order to study the effect of applied potential on morphology of anodized as-deposited aluminum samples, the same electrochemical cell, as described in Figure 26, was employed. The experiments were done in 0.3 M oxalic acid solution at room temperature. The anodization was performed at applied potentials of 10 V, 30 V and 40 V for 30 minutes, respectively, after which the samples were immersed in 5 wt% H_3PO_4 for 60 minutes. The morphology of the AAO template was also studied with a Philips XL30 FEG-SEM. The cross section of the as-deposited aluminum sample at 40 V was observed by SEM after being peeled off.

4.1.3 AAO template fabricated by anodizing electro-polished aluminum

Effects of the smoothness of the surface of aluminum films on anodization are studied. The electrodeposited aluminum samples were first smoothed by electro-polishing in a solution of 60% H_3PO_4 and 40% H_2SO_4 (volume fraction) at 10 V for two minutes at room temperature. This electro-polishing process removes approximately $2 \mu\text{m}$ thick aluminum. Then, the anodization process was carried out with a two-electrode cell, as described in Figure 26, at constant voltage of 30 V in 0.3 M oxalic acid solution at room temperature. When bubbles started to emerge from the bottom of the pores and became progressively intensive, the anodization voltage was

switched off. Mild oxygen bubbling was needed to break down and remove some of the barrier layer. The completion of anodization process could be associated with the color change of the template or the emergence of bubbles from the template surface. After the anodization, one sample was put into the 5 wt.% H_3PO_4 solution for 75 minutes to get the pore bottom opening. Another sample was anodized 40 V in 0.3 M oxalic acid solution with pore widening for 75 minutes. The morphologies of the samples were studied with a Philips XL30 FEG-SEM.

4.2 Results and discussion

4.2.1 Factors affecting on the formation of AAO template

Anodizing time is an important factor for nano-structured palladium membrane fabrication. In order to study the effect of anodizing time, experiments were carried using aluminum foils with changing anodizing time at a constant applied potential of 35 V in 0.3 M oxalic acid solution at room temperature. The results are shown in Figure 27.

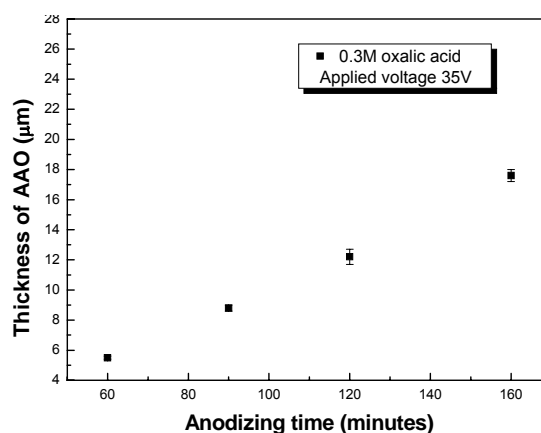


Figure 27 Relationship between anodizing time and thickness of AAO template

It can be seen that the AAO template thickness is proportional to anodizing time. Longer anodizing times can produce thicker AAO templates. However, SEM

observations show that the pore size has no significant change with anodizing time.

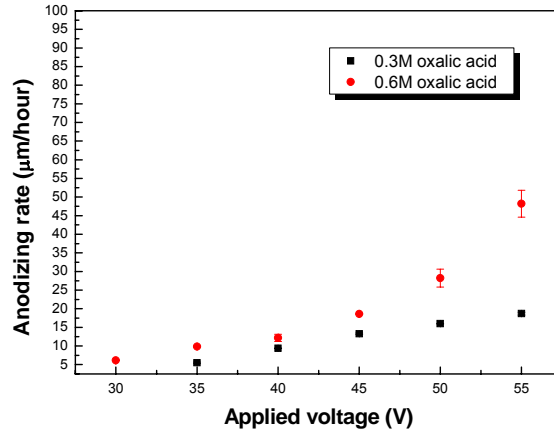


Figure 28 Relationship between anodizing rate and concentration and applied voltage

Other experiments were performed in 0.3 M and 0.6 M oxalic acid solution with changing anodizing voltage to investigate the effects of solution concentration and applied potential in anodizing process. These results shown in Figure 28 demonstrate that the anodizing rate increases linearly with applied voltage, and higher oxalic acid solution concentration can produce faster anodizing rates. SEM images in Figure 29 show that the pore size increases when the applied voltage is increased from 30 V to 55 V in 0.6 M oxalic acid solution at room temperature.

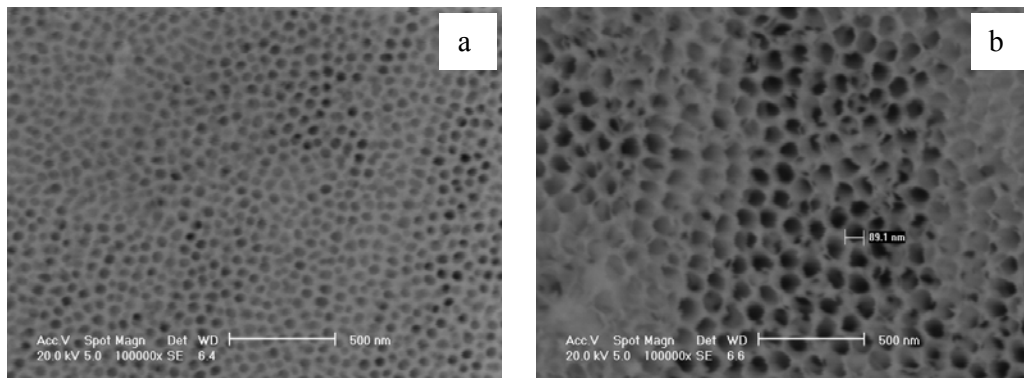
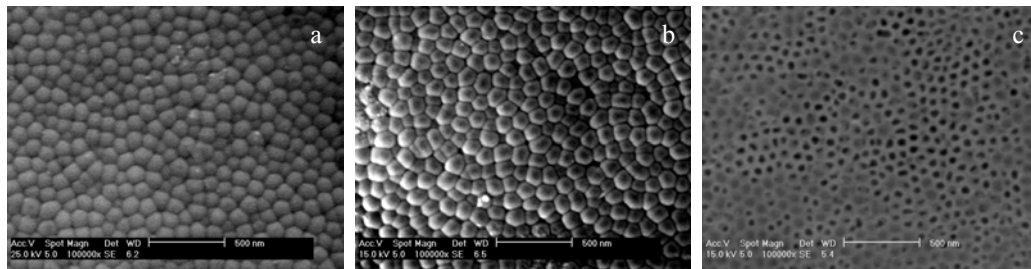


Figure 29 SEM image of AAO in 0.6 M oxalic acid solution; (a) 30 V; (b) 55 V.

4.2.2 Removal of barrier layer on the bottom of the as-prepared AAO template

In order to use AAO template for nano-structured palladium membrane fabrication, the barrier layer on the bottom of the as-prepared AAO template must firstly be removed. Here, we studied the effects of etching time on the removal of barrier layer. In our works, AAO templates obtained by anodizing aluminum foil in a given condition (0.3 M oxalic solution at 35 V voltage and room temperature) were studied. After the aluminum substrate was etched away, the morphology of the pore bottom was semi-spherical, as shown in Figure 30. After 45 minutes etching, the barrier layer at pore bottom was gradually removed. Dark dots can be observed at the pore bottom of each semi-sphere center. After 75 minutes etching, the bottom barrier layer of most pores was removed, and a uniform pore structure was obtained.



(a) No etching

(b) 45 minutes

(c) 75 minutes

Figure 30 Pore bottom opening in a 5 wt. % H_3PO_4 solution

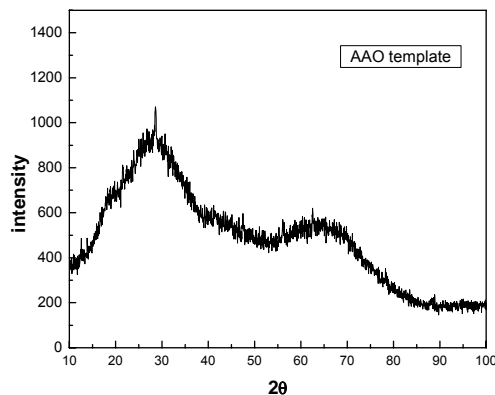


Figure 31 XRD pattern of AAO template

Figure 31 shows the spectrum of the AAO template obtained by X-ray diffraction. In the XRD spectrum, two major peaks were observed: one sharp and strong peak was seen near $2\theta = 30^\circ$, the other small, asymmetric peak near 65° . This XRD spectrum shows an obvious amorphous characteristic.

4. 2.3 Electrochemical behavior in anodization of as-deposited aluminum films

Figures 32, 34 and 35 show the results of measurements of current density vs. time transient for as-deposited aluminum samples at constant 30 volts in 0.3 M oxalic acid solution at room temperature. From the presented graphs, it can be seen that there is a similar change trend no matter what thickness of aluminum samples were used. At the beginning, the current density decreased rapidly to same minimum value, then increased and was kept constant for a certain period of time. In final stage, the current density gradually increased before its value suddenly jumped.

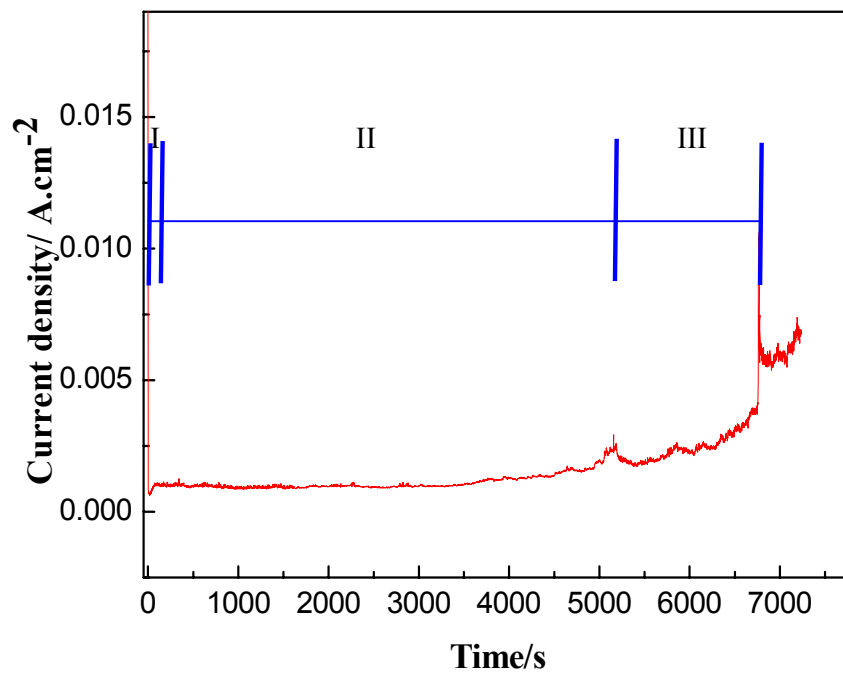
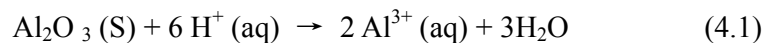


Figure 32 Current density vs. time during anodization of as-deposited 9 μm aluminum

According to Montero-Moreno [45], when an electric field is applied during the anodization process, there is an aluminum oxide layer (barrier layer) firstly formed on the surface of aluminum. The whole process takes place in two steps. In the first step, there is electrical breakdown and the oxide growth. Breakdown occurs when an electric field exceeding the dielectric strength of the oxide is applied across the aluminum film. When this occurs, Al^{3+} ions under the oxide layer will be injected into aluminum at oxide/electrolyte interface, while O^{2-} ions will move to the $\text{Al}_2\text{O}_3/\text{Al}$ metal interface under this high electric field [29]. At this stage the aluminum under the broken-down aluminum oxide thin film will continue to be anodized; resulting in the growth of aluminum oxide. At this stage, the aluminum oxide formation dominates. Ultimately, the aluminum oxide layer becomes sufficiently thick and the breakdown-growth cycle stops. The formation of barrier type aluminum oxide accordingly terminates as well. After this stage, the electrochemically mediated dissolution of aluminum oxide and pore nucleation begins.

Although the barrier oxides are generally very stable, they can still be eroded in the presence of chemicals under the electric field, resulting in pore nucleation. Dissolution of aluminum oxide can be expressed as follows:



During the second step, two opposing processes, the oxide removal at the electrolyte/alumina interface and the oxide growth at the alumina/Al interface, occur and rapidly establish a dynamic equilibrium, resulting in pore deepening. Based on this theory, the measurement of the current density and time curve in anodizing as-deposited aluminum (presented in Figure 32) can be divided into three stages: barrier layer formation and pore nucleation (stage I); pore propagation (stage II); and anodization completion (stage III). During the initial stage of anodization, a thin,

nonporous alumina (Al_2O_3) barrier layer is formed on the top of the aluminum film. In the constant voltage anodization, the current across the anode is inversely proportional to the resistance. Thus, the current density decreases during the initial several seconds when the high resistance barrier layer is formed. As the barrier layer becomes thicker, the resistance at the anode increases, resulting in a decrease in current. When the barrier oxide layer reaches a certain thickness, it stops growing. At this point, the current density shows a minimum value. In the meantime, the pore begins to nucleate as a result of the uneven electric field caused by the surface topography fluctuation that results from the formation of the aluminum oxide layer. An array of pores develops in the barrier layer, the diameters of pores increase until reaching a dimension determined by the anodization conditions (electrolyte, solution type and concentration, anodizing voltage, temperature and etc). Subsequently, the current density starts to increase slightly with the dissolution of the aluminum oxide during the pore nucleation. After reaching a critical value, the pore diameter keeps constant, but the pore depth increases with the anodization time. At this stage, the oxide removal at the electrolyte/alumina interface is dynamically equilibrated with the oxide growth at the alumina/Al interface. The current density remains constant. The pore growth rate is approximately 5-6 $\mu\text{m}/\text{hour}$ at a constant voltage of 30 V with a stable current density. When some of the pores extend to the substrate and the barrier layer is thin enough, the oxygen bubbles start to emerge from the bottom of the pores, and the current density gradually rises. The anodization process should be stopped intensive in order to avoid the “burning” of the alumina template, while mild oxygen is needed to remove at least some of the barrier layer. If the “burning” happens, the current will increase suddenly, as shown in Figure 32. The effect of “burning” on template structure is illustrated in Figure 33. From this SEM image, it can be seen that at this

time, there are some big holes formed in the template although most of the areas still consists of nano-size pores.

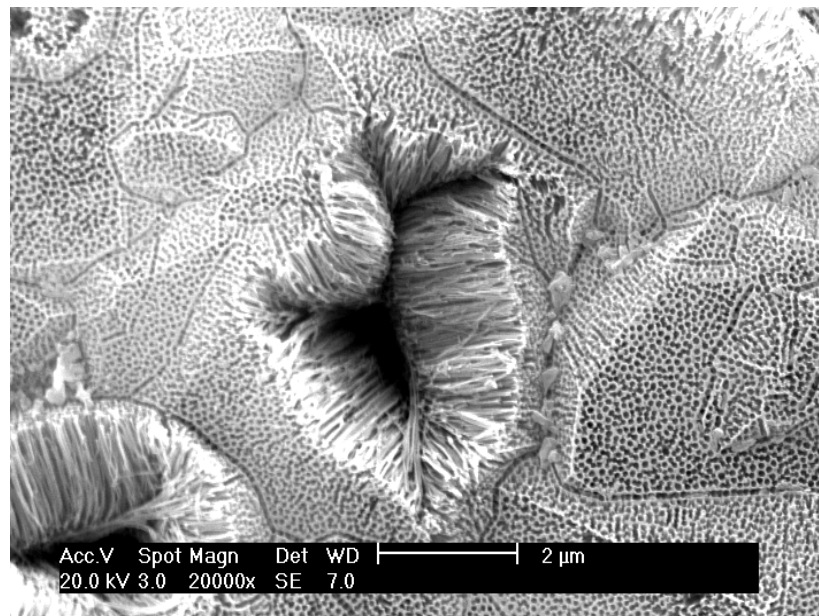


Figure 33 SEM image of template fabrication with “burning”

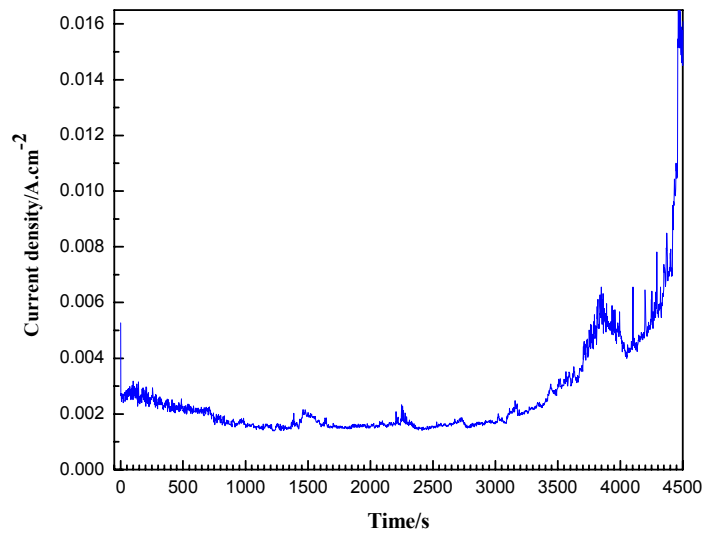


Figure 34 Current density vs. time during anodization of as-deposited 6 μm aluminum

Figures 34 and 35 show the graphs of current density vs. time during anodization of as-deposited aluminum samples with the thickness of 6 μm and 15 μm, respectively.

The similar electrochemical behaviors were observed. In comparison, in the second stage, the process is not very stable (Figure 34). This could be because the as-deposited aluminum membrane is very thin and the period of the stable pore propagation is relatively short, compared with Figure 35. The stable current density-time curves can only be obtained when stable porous film growth occurs in a thicker as-deposited aluminum, as shown in Figure 35.

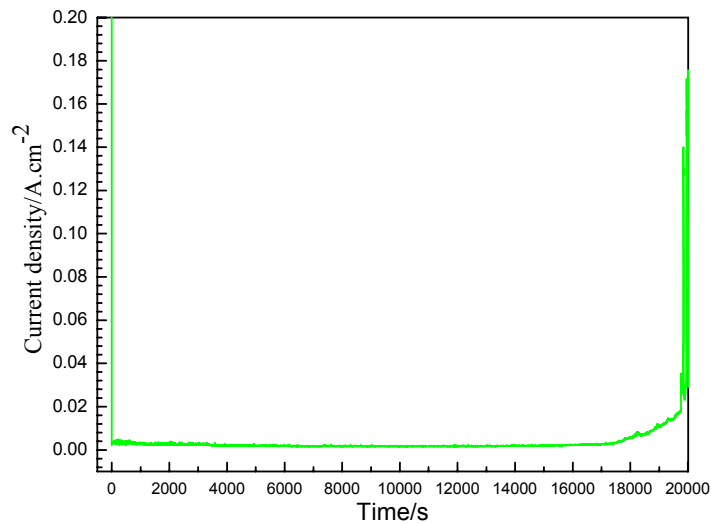


Figure 35 Current density vs. time during anodization of as-deposited 15 μm aluminum

4. 2.4 Morphology of anodized as-deposited aluminum films

In order to achieve ordered nano-pore arrays in as-prepared AAO template, it is highly recommended to pre-texture the sample surface. Many techniques have been used to pre-pattern the surface of aluminum. One technique was introduced by Fournier-Bidoz group [46], in which the aluminum surface is pre-patterned by colloidal crystals. The colloidal crystals were first deposited onto mica using accelerated evaporation induced self-assembly. Then, this mold was imprinted onto an aluminum substrate using a hydraulic press. Another technique used to pre-pattern the aluminum surface is by SiC mold with hexagonally ordered arrays of convexes [47].

Considering the complexity of the process, a well-known two-step anodization technique is a most commonly recommended. A simple anodization imprinting step was used to pre-texture the aluminum surface, as shown in Figure 36, in order to produce hexagonally ordered pores. Actually, the mold used for imprinting is a film of nano-porous alumina produced by first anodization of an aluminum substrate for a time long enough to produce micrometer-sized pores. Then, a chemical-etching step is applied to remove this thin alumina film. The convex pore bottoms of the first anodic alumina film guides the pore formation during the second anodization process to create a template film with ordered hexagonal pore structure.

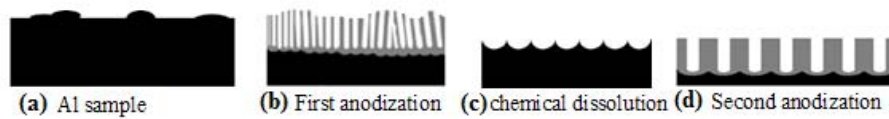


Figure 36 Schematic illustration of two-step anodization pre-pattern process

Figure 37 shows the SEM image of anodized structure of as-deposited aluminum in a 0.3M oxalic acid solution under constant voltage 10 V at room temperature. The SEM image of the template is shown in Figure 38 after pore widening in 5 wt.% H_3PO_4 for 75 minutes. SEM images show that the anodized sample has a very nonuniform pore structure and the original surface morphology of sample become obscure, indicating the erosion rate is very fast, nearly the same both on the surface and the conjunction area among particles.

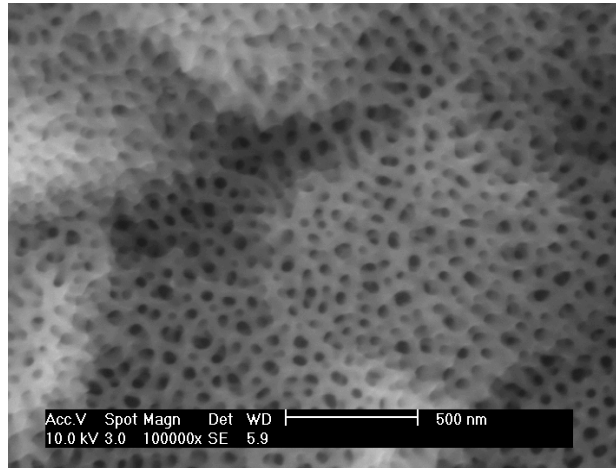


Figure 37 SEM image of anodizing as-deposited aluminum at 10 V

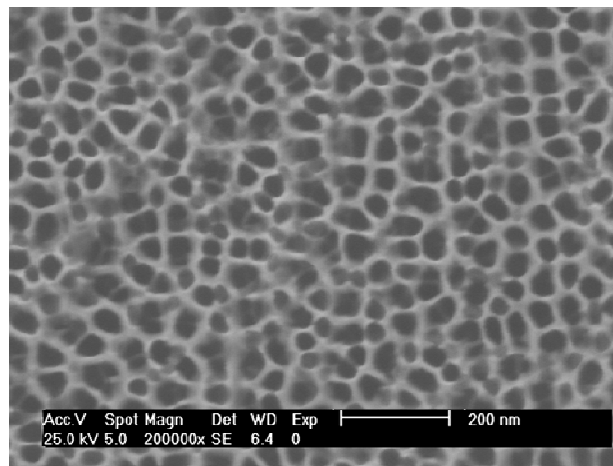


Figure 38 Template obtained after pore widening in 5 wt% H₃PO₄

Figure 39 shows the SEM images from the first anodization of the as-deposited aluminum sample using a 0.3 M oxalic acid solution under constant 30 V after 30 minutes. Compared with Figure 37, a more uniform pore structure was obtained in as-deposited aluminum layer in Figure 39 (a). Under a high magnification in Figure 39 (b) it is observed that the conjunction area among particles had a lower erosion rate compared with the sample anodized at 10 V, indicated by the small erosion region.

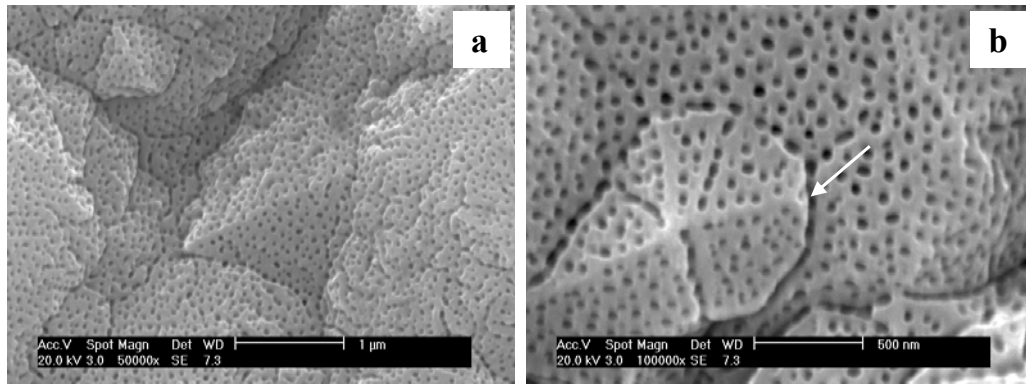


Figure 39 SEM images of anodizing as-deposited aluminum at 30 V

The similar phenomenon was observed by the experiment of anodizing as-deposited aluminum sample with tetragonal particles, as shown in Figure 40. This figure is the SEM image of anodized alumina for 30 minutes in 0.3 M oxalic acid solution at 40 V. From this image, it can be seen that the uniform pores are formed with low erosion rate, indicated by the lowest removal among particles.

Another interesting phenomenon observed in Figure 40 is that the pores are always perpendicular to the surface of grains, which is further confirmed by the cross section SEM image in Figure 41. Pores growth appears to be able to adjust itself according to the surface morphology.

From these three anodization experiments, it can be concluded that low applied potential (10 V) has a faster erosion rate, and produces non-uniform pore structure. The morphology of the as-deposited aluminum has a significant influence on anodization process. As mentioned earlier, there are two processes in anodization process, the oxide removal at the electrolyte/alumina interface and the oxide growth at the alumina/Al interface. Low applied potential might result in a change in equilibrium in the oxide layer formation and dissolution of alumina. The oxide layer formation rate might decrease at low applied potential, while the chemical erosion rate might relatively increase.

As reported by Huang [30], dielectric breakdown always initiates along the local electric field direction, and electrochemical dissolution is also high along the direction of the local maximum electric field. During the early stage, the distribution of electric field is non-uniform on the surface, dependent on the morphology of as-deposited aluminum surface. The low conjunction area among particles has a larger electric field, thus resulting in a faster dielectric breakdown. Since the electrical dissolution is also greater in the local larger electric field area, the barrier layer on the convex parts of the surface becomes thicker than that in the depression. In the area of the flat tetragonal particle facet (Figure 40), the electric field is relatively evenly distributed, resulting in an ordered pore structure perpendicular to the surface along the local field direction. Such an effect is also illustrated in Figure 41. When the morphology changes, the distribution of electric field adjusts itself accordingly, thus resulting in non-ordered nano-pores, as observed in Figure 41.

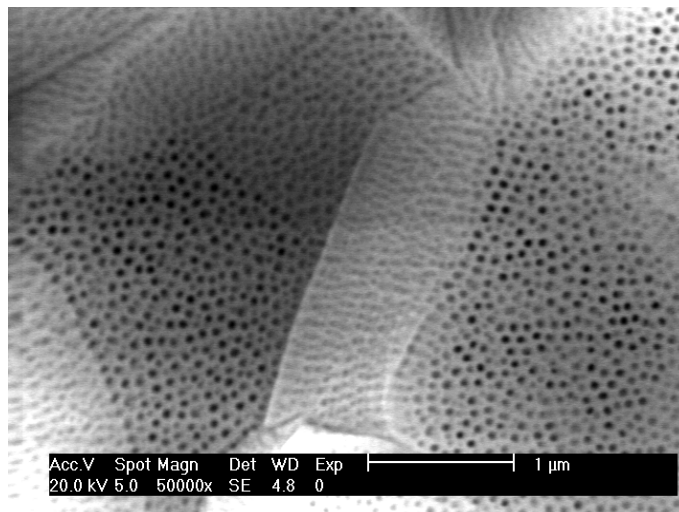


Figure 40 SEM image of anodizing as-deposited aluminum at 40 V

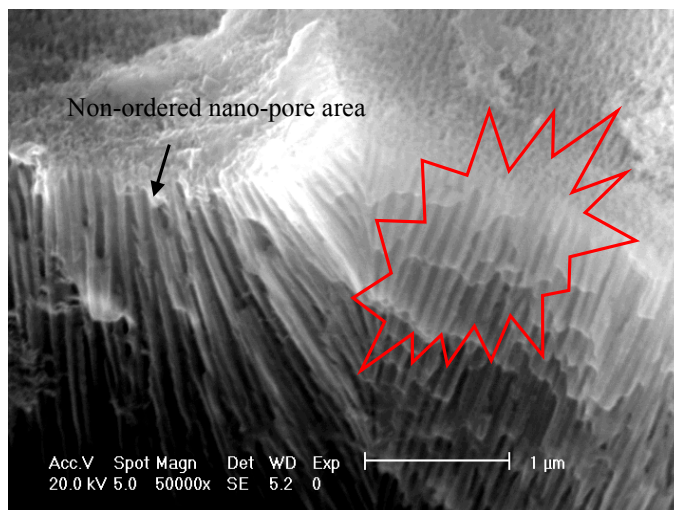


Figure 41 SEM image of the cross section of as-deposited aluminum sample

4.2.5 AAO templates obtained using optimum anodization conditions

From the results given above, we can conclude that direct anodization of as-deposited aluminum film results in relatively uniform pore diameters at 40 V in 0.3 M oxalic acid solution, but the pores are arranged in a relatively disordered way, and are adjusted according to the substrate morphology. A relatively flat surface is the key to obtain well ordered array of nano-pores. Accordingly, a new anodization process was designed, as illustrated in Figure 42. The as-deposited aluminum was first electro-polished to acquire a relatively flat surface sample, and then the electro-polished sample was anodized to obtain an ordered nano-porous structure for nano-structured membrane fabrication.

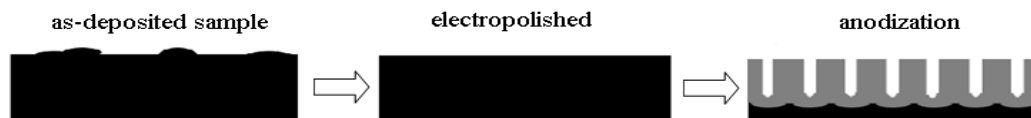


Figure 42 Schematic illustration of obtaining ordered pore in anodization process

Figures 43 and 44 illustrate the SEM images obtained when anodizing electro-polished as-deposited aluminum films at 30 V. Before anodization, the

as-deposited aluminum samples were electro-polished in 40% H_2SO_4 plus 60% (volume fraction) H_3PO_4 solution at 10 V for two minutes. Figure 43 illustrates that a fairly uniform pore diameter was obtained. The cross section SEM image (Figure 44) confirmed that the pores were arranged in a relatively ordered array.

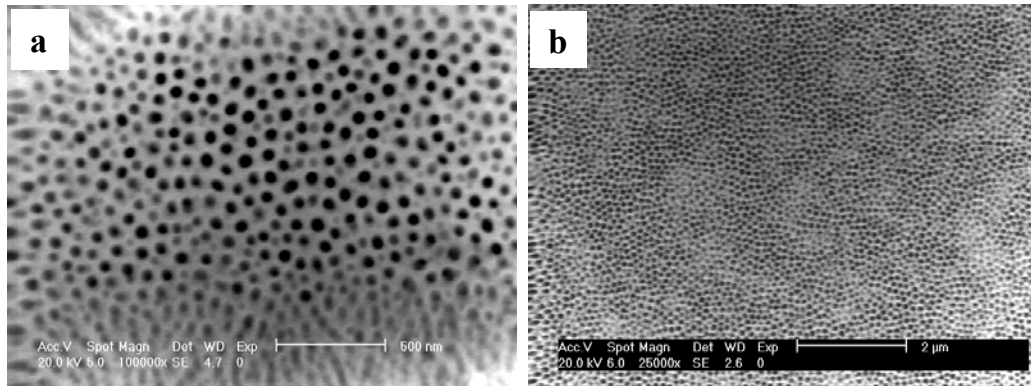


Figure 43 SEM images of template obtained by anodizing electro-polished aluminum

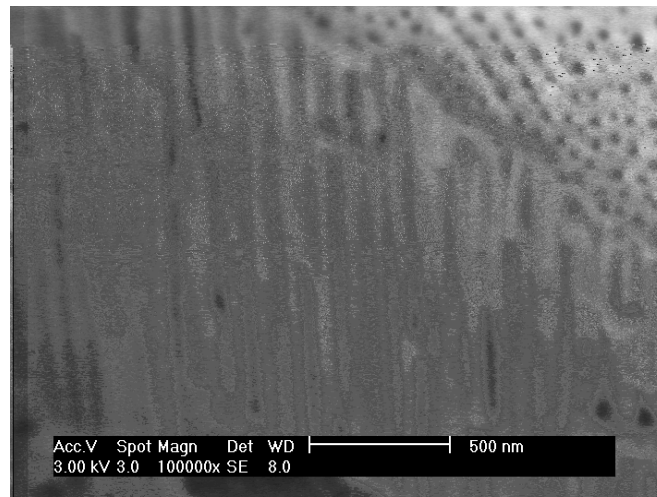


Figure 44 SEM cross section image of anodized electro-polished as-deposited Al

Figure 45 shows the SEM image of the AAO template obtained by anodization of electro-polished as-deposited aluminum using a 0.3 M oxalic acid solution at 40 V and at room temperature. The opening of the pore bottom and the pore widening were

achieved by chemical etching in a 5 wt. % phosphoric acid solution for 75 minutes. From the SEM image, it can be seen that a highly ordered hexagonal template is obtained.

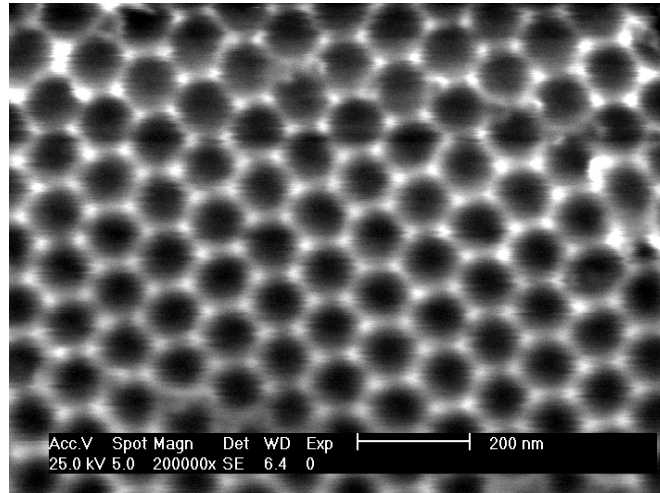


Figure 45 Template from as-deposited aluminum after pore widening

4.3 Summary

In this chapter, we studied the formation of AAO templates using electrodeposited aluminum films and aluminum foils. Results show that the morphology on the surface of the deposited aluminum films has significant influence on the anodization process. An ordered hexagonal pore structure usually forms on flat surface. An uneven dissolution of bottom barrier layer was observed even after 75 minute in 5 wt.% H_3PO_4 solution. Anodization time has no obvious effect on pore structure. Higher applied potential can produce larger and ordered nano-pores. An optimum ordered pore structure can be obtained at 40 V in 0.3 M oxalic acid solution.

CHAPTER 5 Nano-structured Palladium Membranes

Palladium-based membrane free from pinholes can be used to separate hydrogen from mixture of other gases [48]. Palladium membranes can be obtained using various techniques, including electroless plating [49, 50], chemical vapor deposition [51], sputtering [52] and electro-deposition [53-55]. In this chapter, we will use the AAO template to prepare the nano-structured palladium membranes which are of a substantial increase in specific surface area.

Fabrication of nano-structured palladium membrane was performed by electro-deposition using AAO templates obtained by anodization of electroplated aluminum. Considering the unsolved problems existing in fabrication of AAO templates using electrodeposited aluminum, nano-structured palladium membranes were also fabricated by using sputtering method to fill AAO templates prepared using aluminum foils. The preliminary results of hydrogen permeation are analyzed and discussed.

5.1 Experimental procedure

5.1.1 Preparation of palladium membranes using electro-deposition

For electro-deposition of the nano-structured palladium membrane, a solution containing 70 mM K_2PdCl_4 with 20 mM H_2SO_4 was used at room temperature. The potassium tetrachloropalladate powder purchased from Fisher Scientific was used. After dissolution of K_2PdCl_4 in de-ionized water, H_2SO_4 was added to the K_2PdCl_4 solution. Before electro-plating, all the templates were immersed in 5 wt. % H_3PO_4 for 75 minutes to remove the barrier layer at the bottom. Prior to electro-deposition of palladium, the templates were wetted with palladium electroplating solution for 5 minutes to facilitate deposition. Palladium electro-deposition was carried out at 0.3 V

with the template as the cathode, and a platinum wire as the anode.

After the deposition, two-step etching was performed: firstly, the sample was immersed into a 10 wt. % NaOH solution for several seconds. When a small opening was seen to form at the edge, the membrane was gently peeled off. Then, a second etching was performed in a 20% NaOH solution for 3 minute to separate the nano-structured palladium membrane from the template. The morphology of the palladium membrane was examined with a Philips XL30 FEG-SEM and an EDS Analyzer Scan Generator EDI-2.

5.1.2 Preparation of nano-structured palladium membranes using sputtering

The deposition of palladium was performed using a Hammer VI Sputter Coater with pure palladium target. A current of 10 milliamp and vacuum of 70 millitorr was used with the sputtering times of 20, 30, 40, 50 and 60 minutes with 5 minute break between each intervals. The AAO templates were formed in 0.3 M oxalic acid at 40 V using Al foils. The morphology and cross section of all the samples were analyzed using a Philips XL30 FEG-SEM.

5.1.3 Hydrogen permeation test on sputtered palladium membranes

The setup used for the hydrogen permeation test is illustrated in Figure 46. The ratio of hydrogen to nitrogen was adjusted by the mass flow control system. Then, the gas mixture was injected into the permeation cell. The temperature of the gas was controlled by the temperature control system connected to the furnace. In order to get a homogeneous gas flow inside the permeation cell, two gas input sites were introduced into the permeation cell, as shown in Figure 47. The palladium membranes was supported by a stainless steel mesh set inside the permeation cell, through which all the gas could pass with a certain resistance. The sealing was performed by a

graphite gasket inside the permeation cell. After the hydrogen separation, the gas fled into a gas flow meter to measure the permeation rate. The purity of hydrogen was tested by gas chromatography.

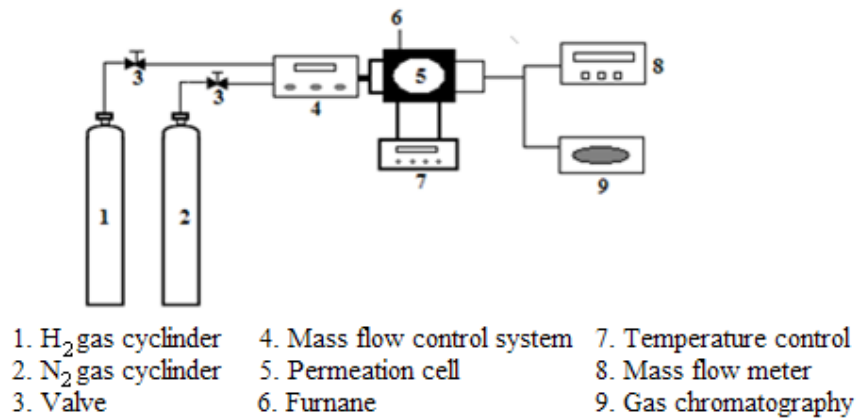


Figure 46 Schematic diagram of experimental setup for hydrogen permeation test

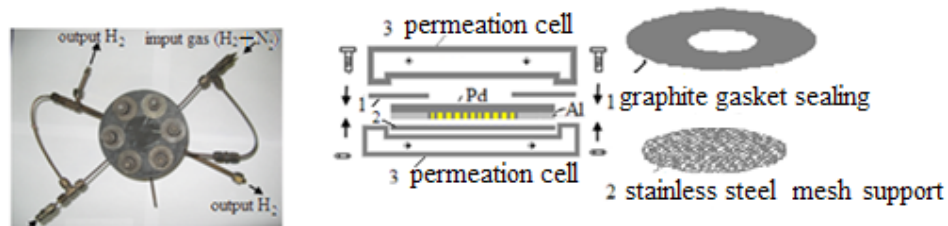


Figure 47 Schematic illustrations of hydrogen permeation cell and inside sealing

Before each test, the palladium membrane was tested using nitrogen gas to ensure there was no leakage of the membrane. The hydrogen permeation test was performed on the sputtered palladium membrane on an AAO template at increasing temperatures (150, 200, 250, 300, 350 and 400°C). It was found that fast rate of temperature increase would produce cracking, and lead to membrane failure. An optimum temperature increasing rate was 1 °C/min.

After the hydrogen permeation test, the sample structure was analyzed by a rotating anode Rigaku X-ray generator and the morphology of palladium membrane

was observed using a Philips XL30 FEG-SEM.

A major problem encountered with the sputtered palladium membrane was the brittleness resulting from the AAO templates, which cannot withstand high mechanical stress associated with the sealing process. This could be solved by two ways: Al-Pd/AAO jointed by ceramic glue sealing, and Al-AAO self-sealing, as shown in Figure 48.

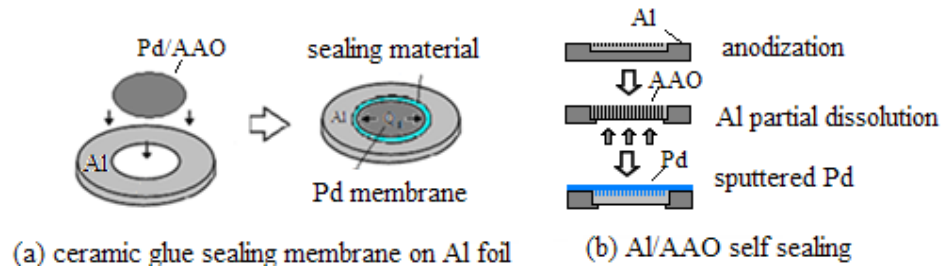


Figure 48 Schematic sketch of palladium membrane sealing in hydrogen permeation

One sealing method involved connecting the palladium membrane to a piece of aluminum foil which had a hole (diameter: $\varnothing_1 = 8$ mm) in the middle. The palladium membranes were fabricated as follows: firstly, a piece of aluminum foil was anodized in 0.3 M oxalic acid at 40 V for 3 hours in an anodization cell with a diameter of $\varnothing_1 = 10$ mm, after which the remaining aluminum at the back was dissolved in SnCl_4 . Then, the template was immersed into a 5 wt. % H_3PO_4 solution for 75 minutes to let the pore bottom open. The sputtering deposition was performed for 60 minutes with pure palladium target. Then the palladium membrane was connected to a piece of aluminum by a ceramic sealing glue called Resond 907 Red Thread Locking and Pipe, which can withstand the temperatures from -150°C to 1150°C .

The second sealing method is of the unique advantage of natural connection between anodic alumina and aluminum. The process of palladium membrane fabrication is shown in Figure 49. Firstly, anodization of aluminum was performed on a piece of $25\ \mu\text{m}$ thick aluminum foil in an anodization cell with a 10 mm diameter

hole (\O_1) using a 0.3 M oxalic acid solution at 40 V. After two hours of anodization, an AAO template with a thickness of about 12 μm was embedded inside the aluminum foil. Then, the anodization cell was disconnected and a dissolution cell with a 6 mm diameter (\O_2) exposure area was attached to the anodization cell, as illustrated Figure 49 (b), in order to dissolve the remaining un-anodized aluminum in the SnCl_4 solution. For application of this method, the rubber O-rings used for the sealing of the two cells was a key. Any leakage will lead to the formation of small pores in the aluminum, resulting in the failure of the template fabrication. After each anodization experiment, the O-rings had to be changed. Once a good AAO template was achieved, sputtering was performed on the whole sample by Sputter Coater.

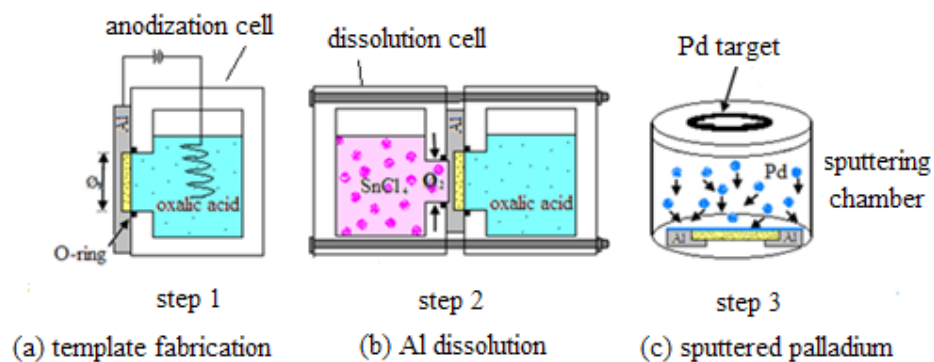


Figure 49 Schematic illustration of self-sealing palladium membrane fabrication

5.2 Results and discussion

5.2.1 Formation of nano-structured palladium membrane by electro-deposition

The fabrication process of a nano-structured palladium membrane by electro-deposition is illustrated in Figure 50. Firstly, the AAO template was fabricated by anodization of electroplated aluminum. After removing the barrier layer on the bottom using a 5 wt% H_3PO_4 solution, palladium was electroplated in the AAO template, followed by a two-step etching procedure to release the free-standing nano-structured palladium membrane.

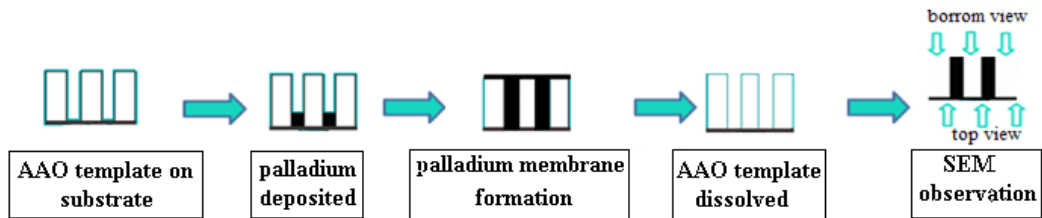
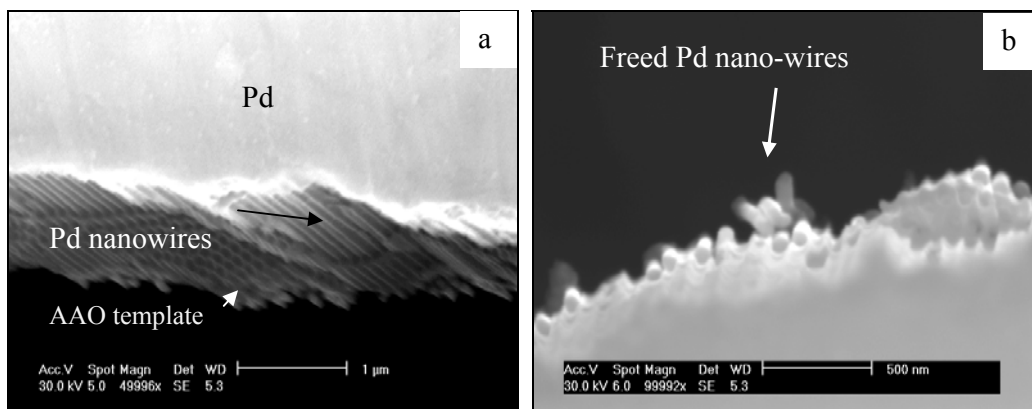


Figure 50 Schematic graph of fabrication process of electro-deposited Pd membrane

The two-step etching was performed as follows: the sample was firstly immersed in a 10 wt.% NaOH solution for several seconds. When a small opening formed at the edge, the membrane was gently peeled off. Figure 51 shows the SEM images of the top and side views of palladium membrane fabricated by electro-deposition after being removed from the substrate. For the top view of the displayed area, it can be seen that palladium deposited into the pores of AAO template. This result is further confirmed by the cross section SEM image shown in Figure 51 (b). From the broken sample at the edge area, it can be clearly seen that the electrodeposited wires were embedded in the template.

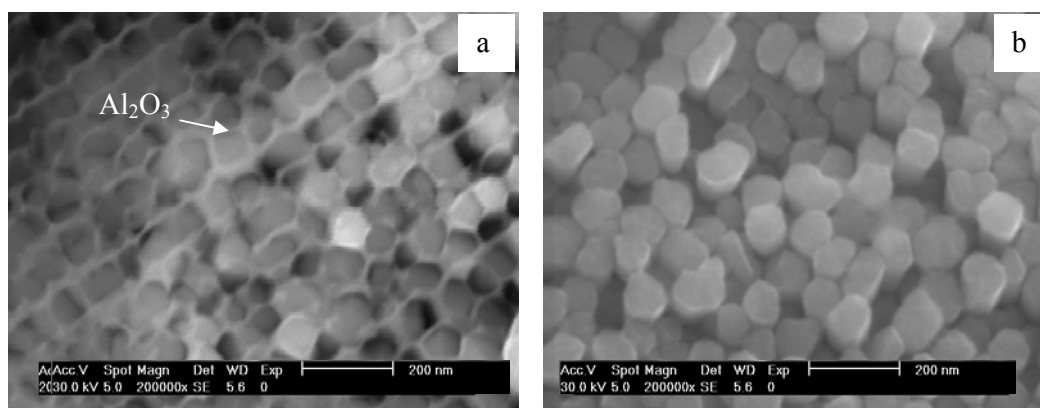
A second etching was performed in a 20 wt.% NaOH solution to release the nano-structure. Figure 52 shows the SEM images of the bottom view of the electroplated palladium membrane before and after the second etching. It can be seen that before the second etching, the anodic alumina template was still visible between the palladium nano-wires (see Figure 52 (a)). After the second etching was performed, the sample was immediately rinsed in water and dried. The SEM image seen in Figure 52 (b) was taken after this process was completed. When compared with the SEM image taken before etching, it can be seen that all the palladium nano-wires were released from the template.



(a) Top view

(b) Cross section

Figure 51 SEM images of removed nano-structured Pd membrane embedded in AAO



(a) Before second etching away AAO template

(b) After second etching

Figure 52 SEM images of nano-structured palladium membrane bottom view

The cross section of the nano-structured palladium membrane after the second etching is shown in Figure 53. One can see that the palladium nano-wires freely stand on the palladium membrane. EDS analysis displayed that only Pd peaks and no Al or O peaks were present, indicating that the membrane only consisted of pure palladium.

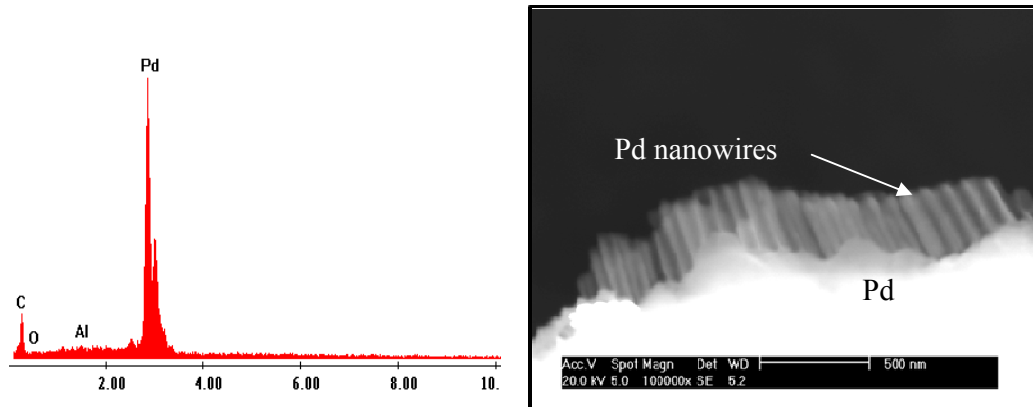
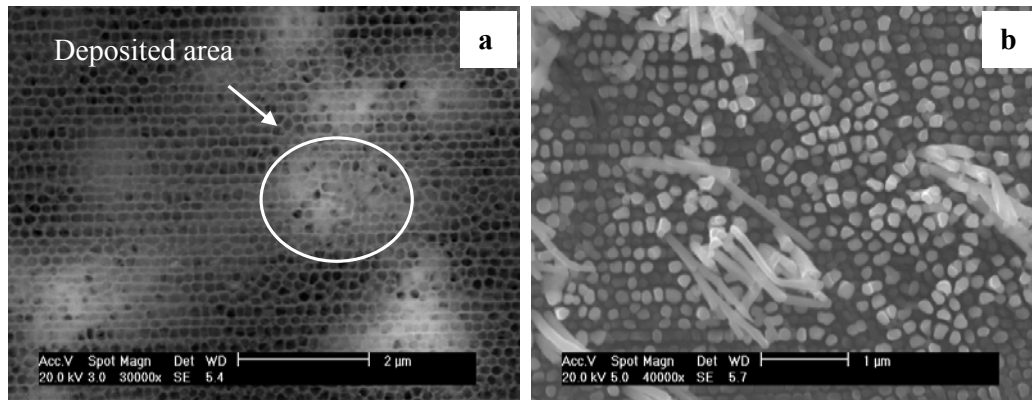


Figure 53 EDS spectrum and SEM image of freed electro-deposited Pd membrane

5.2.2 Possible prospect and currently existing problems

5.2.2.1 Uneven deposition of palladium



(a) Top view of Pd nano-wires in template (b) After dissolution of the template

Figure 54 SEM images of unevenly electro-deposited palladium membrane.

In the process of electroplating palladium, one problem to be solved is the inconsistent and uneven deposition caused by the uneven dissolution of the barrier layer at the bottom of the AAO template. As shown in Figure 54, after 10 minutes of deposition, some area already started to form nano-wires, while in other area, nano-wires was not observed yet. This phenomenon was further confirmed after the

dissolution of the alumina template. Long nano-wires were observed to be randomly distributed.

5.2.2.2 Cracking phenomenon

In order to obtain more even deposition of palladium, the electro-deposition voltage was increased in order to induce the breakdown of the barrier layer. The SEM image of such a sample is shown in Figure 55. Increasing the deposition voltage can partly solve the uneven deposition problem; however, it will cause cracking. These cracks might be induced by higher local temperature during deposition. Only when uneven deposition problem is solved, the porous anodic aluminum oxide template can be effectively used for the preparation of electro-deposited nano-structured palladium membranes.

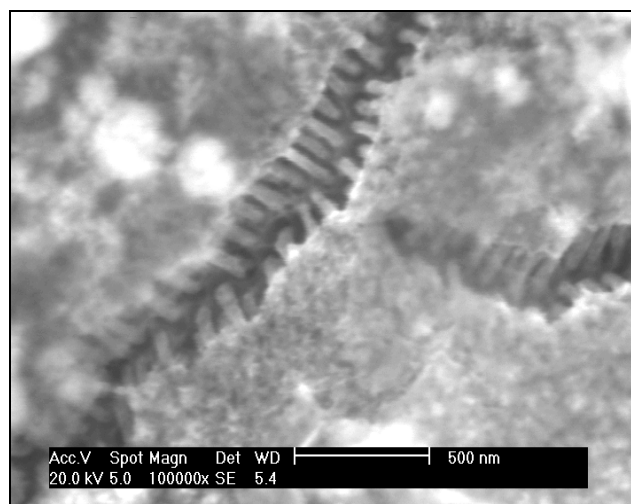


Figure 55 SEM image of cracking in electroplated Pd membrane at high potential

5.2.3 Formation of nano-structured palladium membrane by sputtering

Figure 56 shows the SEM images of sputtered palladium membranes deposited on AAO templates with sputtering time of 40, 50 and 60 minutes , respectively. Also

shown is the cross section SEM image for sputtering of 60 minutes. As observed by SEM, palladium particles were clustered on the AAO template after 20 minutes of sputtering, and many pores in the AAO template were still visible. When the sputtering time was increased to 40 minutes, the AAO template was covered with palladium. However, from EDS spectrum shown in Figure 57 (a), it can be seen that Al K_{α} peak was still present in the spectrum, indicating that the palladium layer does not completely cover the AAO template.

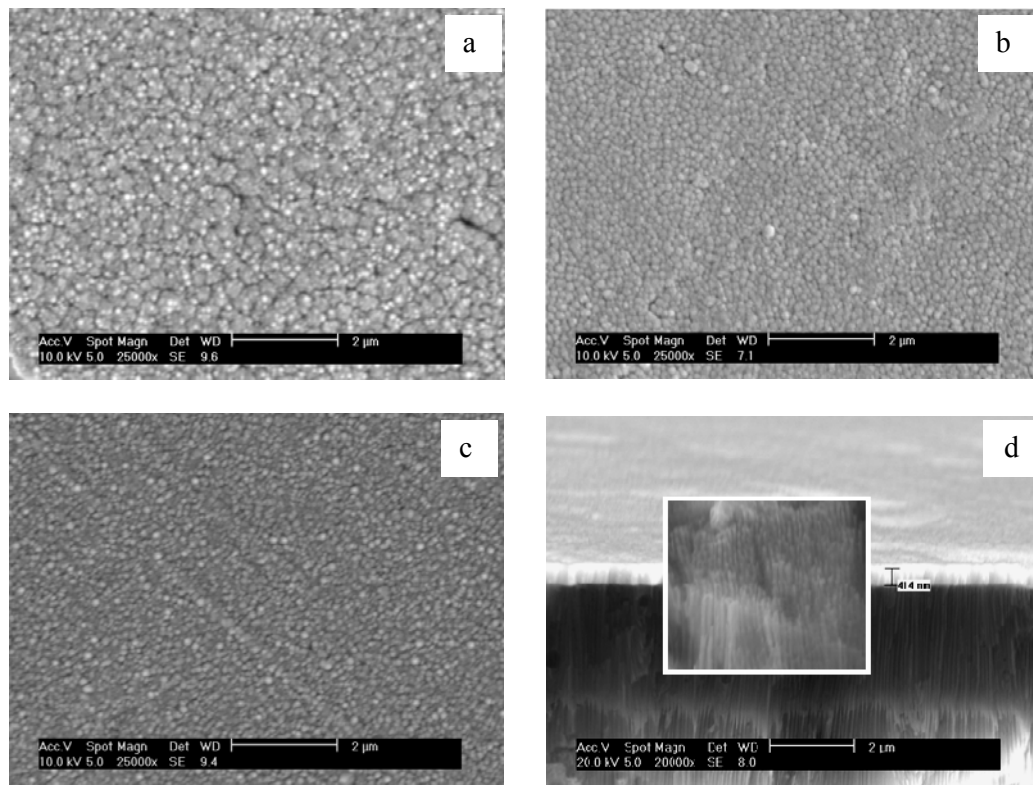


Figure 56 SEM image of palladium membrane fabrication with deposition time. (a) 40 minutes; (b) 50 minutes; (c) 60 minutes; (f) cross section.

With increasing depositing time, palladium membrane thickness increases. When the sputtering time was increased to 50 minutes, no Al K_{α} peak was observed, seen in Figure 57 (b), indicating a homogeneous palladium membrane was formed and the AAO template was completely covered with palladium. After 60 minutes, a

homogenous membrane was formed with small particle size, as illustrated by SEM images in Figure 56 (c). From the cross section SEM image of the palladium membrane with 60 minutes deposition time (Figure 56 (d)), it can be seen that pores in the AAO template were filled with palladium and a nano-structured palladium layer was formed.

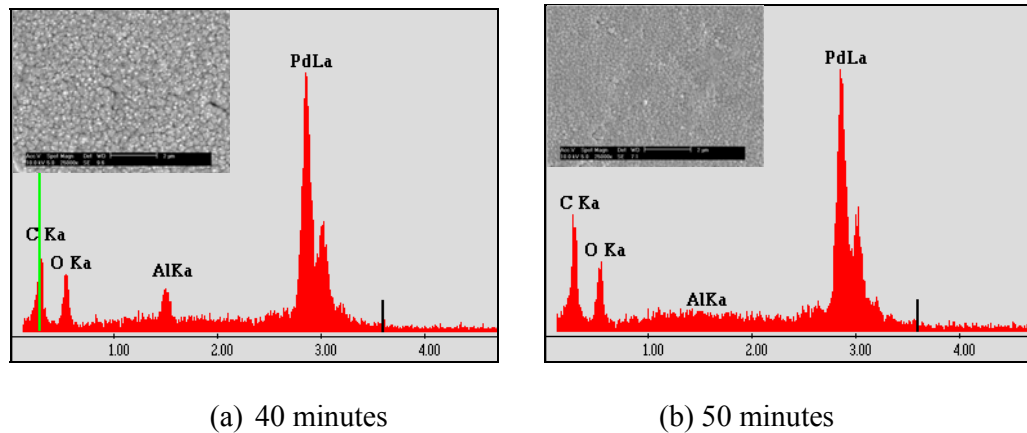


Figure 57 EDS spectrums of Pd membranes after 40 and 50 minutes sputtering

5.2. 4 Hydrogen permeation test of as-prepared palladium membranes

Two methods can be used for membrane sealing: Al-Pd/AAO membrane glue sealing and Al-AAO self-sealing. Comparing between this two methods, it can be concluded that for Al-Pd/AAO glue sealing, special care had to be taken when applying the ceramic glue. Too much glue may block the membrane surface, while too little glue may lead to the sealing failure. For the Al-AAO self-sealing membranes, the O-rings in the cells were a key for the membrane fabrication. Any leakage of anodization solution could lead to the failure of membrane fabrication.

Hydrogen permeation tests were performed at 150, 200, 250, 300, 350 and 400°C. The results are shown in Figure 58. It is seen that hydrogen permeation rate linearly increases with temperature. When temperature reaches a critical point (300°C), a sudden abnormal increase of hydrogen flux was observed. This phenomenon would be

due to the different thermal expansion coefficients between the palladium membrane and the AAO template. With increasing temperatures, higher stress might be induced between the palladium membrane and the AAO template and result in the crack formation in the Pd membrane.

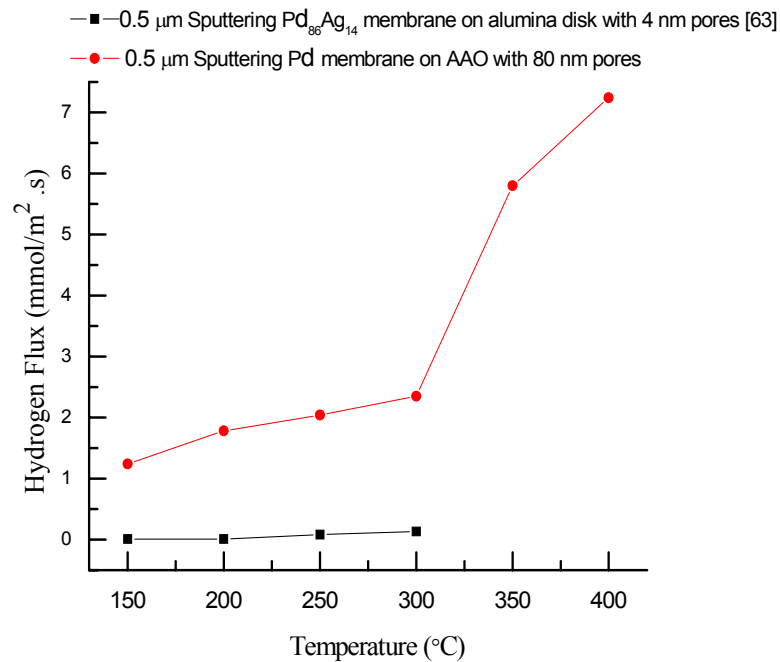


Figure 58 Hydrogen permeation rate vs. temperature performed on sputtered Pd

The results of hydrogen flux on sputtering 0.5 μm Pd₈₆Ag₁₄ membrane [56] were shown in the same figure for comparison. It is seen that there is an obvious increase in hydrogen flux for nano-structured palladium membranes. Hydrogen permeation flux of sputtered nano-structured palladium membranes is over 10 times higher than the Pd₈₆Ag₁₄ membrane at 150 °C. This increase may be attributed to the increased surface area of the membranes. As described in literature review, at low temperatures the surface processes are the rate-determining step. An increase in area of contact surface will substantially speed up the hydrogen permeation rate.

The microstructure of the palladium membrane after the hydrogen-permeation test at 400 °C was observed using SEM and the result was shown in Figure 59. Many tiny cracks were found in the palladium membrane which is consistent with the results obtained from the hydrogen permeation tests. The gas chromatography analysis conducted on separated gas showed that the nitrogen gas was present, indicating that the leakage occurred in the membrane.

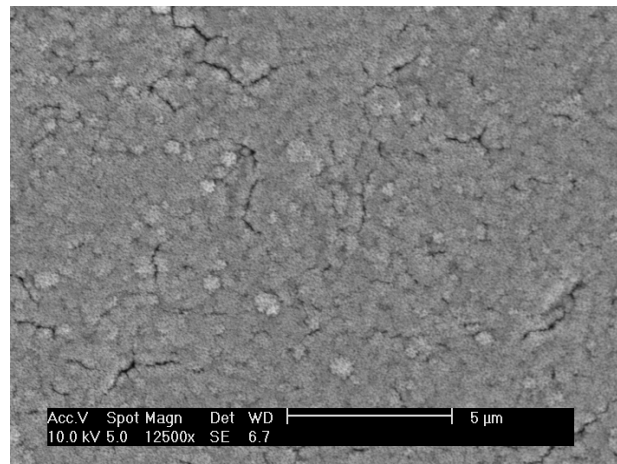


Figure 59 SEM image of sputtered Pd membrane after hydrogen permeation

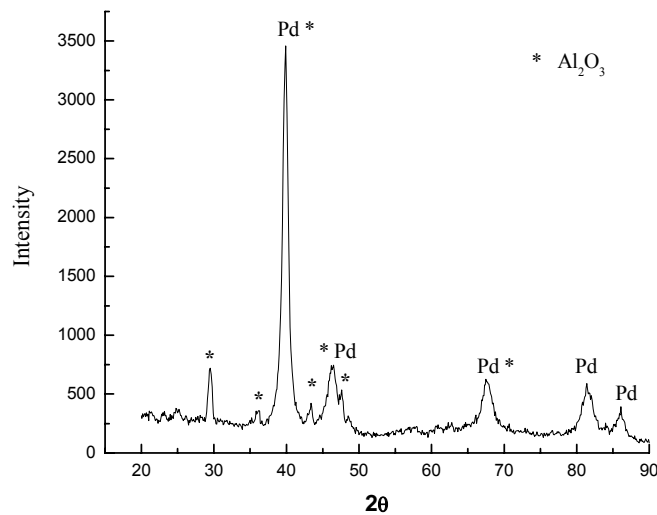


Figure 60 XRD pattern for sputtered palladium sample after hydrogen permeation

XRD analysis was performed on the sputtered palladium on the AAO template after the hydrogen permeation test at 400 °C and the result is shown in Figure 60. The diffraction peaks appear at 2θ of 40.12°, 46.7°, 68.09°, 82.10°, 86.8°, corresponding to (111), (200), (220), (311), (222) planes of the palladium crystal, respectively. In addition, crystalline peaks of Al₂O₃ were also observed. Since the anodic alumina template shows amorphous Al₂O₃ structure before hydrogen permeation test, as shown in Figure 31, this means that hydrogen permeation may induce AAO template transform from the amorphous to a crystalline state. Since the temperature of hydrogen permeation test (400 °C) is far less than the crystallization temperature required for amorphous state of Al₂O₃, the reason for this phase transformation is still unclear.

5.3 Summary

In this chapter, we studied the preparation of nano-structured palladium membranes by using the AAO template obtained in the last chapter and the possible application for hydrogen separation. Two methods, sputtering and electro-deposition were used for filling palladium into the holes of AAO template. Our results show that the palladium membrane prepared by sputtering is of good properties for hydrogen separation at temperature below 300°C. However, for palladium membranes prepared by electro-deposition, due to the formation of uneven deposition and cracks, their application for hydrogen separation is still not feasible at present. Based on the studies of palladium membrane prepared by sputtering, it is indicated that the electro-deposition of nano-structured palladium is very promising in the field of hydrogen separation if the problems of formation of uneven deposition and cracks are resolved. The great enhancement of hydrogen separation in nano-structured palladium

membranes is due to substantial increase in the specific surface area of membranes.

CHAPTER 6 Conclusions

In this thesis, nano-structured palladium membranes were fabricated using an AAO-template-assisted method. Templates were obtained by anodizing electro-deposited aluminum films and aluminum foils. The mainly results are given as follows:

- The AlCl_3 and LiAlH_4 concentrations have different influences on covering power of the formation of aluminum film. The AlCl_3 concentration may significantly increase covering power, while this phenomenon is not obvious for LiAlH_4 concentration. But the increase of LiAlH_4 concentration causes an increase of particle size in the deposited aluminum. The optimum ratio of AlCl_3 to LiAlH_4 for the formation of aluminum film is in the range from 3:1 to 4:1.
- Applied potential also has an important influence on the microstructure of as-prepared aluminum films. The optimum potentials obtained in our experiments are in the range from -3 V to -4 V.
- The as-prepared polycrystalline aluminum film has a very weak (111) texture, which results from the different surface free energies in different crystalline planes of aluminum.
- The morphology of the as-deposited aluminum sample can greatly affect the anodization process. In general, an ordered pore arranging in hexagonal structure form on the smooth surface of aluminum films.
- The increase in anodization time allows producing thicker template but the pore size keeps constant.
- The oxalic acid solution concentration can increase the anodizing rate. The similar effect is also found in applied voltage. Moreover, larger applied

voltage produces more ordered AAO template.

- An uneven etching was observed after 75 minutes in a 5 wt.% H_3PO_4 solution and the removal of the barrier layer on the bottom of as-prepared AAO templates started after 45 minute.
- The as-prepared AAO templates mainly consist of amorphous Al_2O_3 .
- The palladium membrane prepared by sputtering shows a good property for hydrogen separation. This is due to the increase in specific surface area of nano-structured palladium membranes. But the formation of cracks in the evaluated temperature will result in the failure of hydrogen separation at the temperature above 300 °C.
- Uneven dissolution of the barrier layer in the AAO template may induce an uneven deposition of palladium, which will restrict the application of nano-structured palladium membrane for hydrogen separation. If this problem is solved in the works in the future, electro-deposited nano-structured palladium membrane prepared using the porous anodic aluminum oxide template should be also of good properties for hydrogen separation and purification.

References

1. N. Itoh, W.C.X., *Selective hydrogenation of phenol to cyclohexanone using palladium-based membranes as catalysts*. Applied Catalysis A: General, 1993. **107**(1): p. 83-100.
2. Collins, J.P. and J.D. Way, *Preparation and Characterization of a Composite Palladium-Ceramic Membrane*. Industrial & Engineering Chemistry Research, 1993. **32**(12): p. 3006-3013.
3. Uemiya, S., T. Matsuda, and E. Kikuchi, *Hydrogen Permeable Palladium Silver Alloy Membrane Supported on Porous Ceramics*. Journal of Membrane Science, 1991. **56**(3): p. 315-325.
4. Uemiya, S., et al., *Separation of Hydrogen through Palladium Thin-Film Supported on a Porous-Glass Tube*. Journal of Membrane Science, 1991. **56**(3): p. 303-313.
5. Shi, D., *Functional thin films and functional materials : new concepts and technologies*. 2003, New York, Springer. p. 39
6. Mulder, M., *Basic Principles of Membrane Technology*, ed. s. edition. 1996: Dordrecht ; Boston : Kluwer Academic. 227.
7. Chik, H. and J.M. Xu, *Nanometric superlattices: non-lithographic fabrication, materials, and prospects*. Materials Science & Engineering R-Reports, 2004. **43**(4): p. 103-138.
8. Baker, R.W., *Membrane thcnology and applications*. second edition ed. 2004: John Wiley & Sons Ltd, The Artrium, Southern Gate, Chichester, West Sussex, England.
9. Huang, T.C., M.C. Wei, and H.I. Chen, *Permeation of hydrogen through*

- palladium/alumina composite membranes*. Separation Science and Technology, 2001. **36**(2): p. 199-222.
10. Nam, S.E. and K.H. Lee, *A study on the palladium/nickel composite membrane by vacuum electrodeposition*. Journal of Membrane Science, 2000. **170**(1): p. 91-99.
 11. Uemiya, S., Kude Y, Sugino K., Sato, N., *A Palladium/Porous-Glass Composite Membrane for Hydrogen Separation*. Chemistry Letters, 1988. **10**: p. 1687-1690.
 12. Uemiya, S., Matsuda T., KiKuchi E., *Aromatization of Propane Assisted by Palladium Membrane Reactor*. Chemistry Letters, 1990. **8**: p. 1335-1338.
 13. Itoh, N., et al., *Deposition of palladium inside straight mesopores of anodic alumina tube and its hydrogen permeability*. Microporous and Mesoporous Materials, 2000. **39**(1-2): p. 103-111.
 14. Govind, R. and D. Atnoor, *Development of a Composite Palladium Membrane for Selective Hydrogen Separation at High-Temperature*. Industrial & Engineering Chemistry Research, 1991. **30**(3): p. 591-594.
 15. Shu, J., B.P.A. Grandjean, and S. Kaliaguine, *Asymmetric Pd-Ag Stainless-Steel Catalytic Membranes for Methane Steam Reforming*. Catalysis Today, 1995. **25**(3-4): p. 327-332.
 16. Jemaa, N., et al., *Thin palladium film formation on shot peening modified porous stainless steel substrates*. Industrial & Engineering Chemistry Research, 1996. **35**(3): p. 973-977.
 17. Chae, H.T., et al., *Irradiation tests for U3Si-Al dispersion fuels with aluminum cladding*. Journal of Nuclear Materials, 2008. **373**(1-3): p. 9-15.
 18. Eckert, J., *Electrode kinetics of the aluminium deposition from tetrahydrofuran*

- electrolytes* Electrochimica Acta, 1981. **26**(8): p. 1169-1175.
19. M. GÁLOVÁ, D.K.L.a.L.L., *Basic Parameters of the Electrode Process of Aluminum Deposition from Tetrahydrofuran Solutions I: exchange current density*. Surface Technology, 1980. **11**(5): p. 371-376.
 20. Lefebvre, M.C. and B.E. Conway, *Al-27 NMR spectroscopy studies on speciation of Al complex ions in AlCl₃+LiAlH₄ solutions in tetrahydrofuran for electroplating of Al*. Journal of Electroanalytical Chemistry, 1998. **448**(2): p. 217-227.
 21. GÁLOVÁ, M., *Electrodeposition of aluminium from organic aprotic solvents*. Surface Technology, 1980. **11**(5): p. 357-369.
 22. Galova, M., D. Kladekova, and L. Lux, *Basic Parameters of the Electrode Process in Aluminum Deposition from Tetrahydrofuran Solutions .2. Mechanism of the Electrode-Reaction*. Surface Technology, 1981. **13**(4): p. 315-324.
 23. Badawy, W.A., B.A. Sabrah, and N.H.Y. Hilal, *A New Bath for the Electrodeposition of Aluminum .2. Kinetics and Mechanism of the Deposition and Dissolution Processes*. Journal of Applied Electrochemistry, 1987. **17**(2): p. 357-369.
 24. Lefebvre, M.C. and B.E. Conway, *Nucleation and morphologies in the process of electrocrystallization of aluminium on smooth gold and glassy-carbon substrates*. Journal of Electroanalytical Chemistry, 2000. **480**(1-2): p. 46-58.
 25. S. Fournier-Bidoz , V.K., D. Routkevitch , I. Manners, G. A. Ozin, 2004. *Advance Materials, Highly Ordered Nanosphere Imprinted Nanochannel Alumina (NINA)*. **16**(23-24): p. 2193-2196.
 26. Brace, A.W., *The Technology of Anodizing Aluminum*. Third ed. 2000: Modena,

Italy : Interall S.r.l.

27. O Jessensky, F.M., U Gösele, *Self-Organized Formation of Hexagonal Pore Structures in Anodic Alumina*. Journal of The Electrochemical Society, 1998. **145**(11): p. 3735-3740.
28. Shershulsky, V.P.P.a.V.I., *Theoretical modelling of porous oxide growth on aluminum*. Journal of physics D: Applied physics 1992. **25**(8): p. 1258-1263.
29. Z. Wu, C.R., and L. Menon, *A Study of Anodization Process during Pore Formation in Nanoporous Alumina Templates*. Journal of The Electrochemical Society, 2007. **154**(1): p. E8-E12.
30. Huang, Q., W.K. Lye, and M.L. Reed, *Mechanism of isolated pore formation in anodic alumina*. Nanotechnology, 2007. **18**(40): p. -.
31. Lin, S.W., et al., *Fabrication and magnetic properties of nickel nanowires*. Journal of Magnetism and Magnetic Materials, 2004. **282**: p. 28-31.
32. Palibroda, E., et al., *Aluminum Porous Oxide-Growth - on the Electric-Conductivity of the Barrier Layer*. Thin Solid Films, 1995. **256**(1-2): p. 101-105.
33. Yu, W.H., et al., *Influence of defects on the ordering degree of nanopores made from anodic aluminum oxide*. Physics Letters A, 2006. **350**(5-6): p. 392-395.
34. Das, B., *Investigation of nanoporous thin-film alumina templates*. Journal of the Electrochemical Society, 2004. **151**(6): p. D46-D50.
35. O. Jessensky, F.M.a.U.G., *Self-Organized Formation of Hexagonal Pore Structures in Anodic Alumina*, in *Journal of the Electrochemical Society*. 1998. p. 3735-3740.
36. Nielsch, K., et al., *Hexagonally ordered 100 nm period nickel nanowire arrays*. Applied Physics Letters, 2001. **79**(9): p. 1360-1362.

37. Zheng, M., et al., *Magnetic properties of Ni nanowires in self-assembled arrays*. Physical Review B, 2000. **62**(18): p. 12282-12286.
38. Saito, M., et al., *Micropolarizer Made of the Anodized Alumina Film*. Applied Physics Letters, 1989. **55**(7): p. 607-609.
39. Preston, C.K. and M. Moskovits, *Optical Characterization of Anodic Aluminum-Oxide Films Containing Electrochemically Deposited Metal Particles .I. Gold in Phosphoric-Acid Anodic Aluminum-Oxide Films*. Journal of Physical Chemistry, 1993. **97**(32): p. 8495-8503.
40. Li, Y., et al., *Ordered semiconductor ZnO nanowire arrays and their photoluminescence properties*. Applied Physics Letters, 2000. **76**(15): p. 2011-2013.
41. Konno, M., et al., *A Composite Palladium and Porous Aluminum-Oxide Membrane for Hydrogen Gas Separation*. Journal of Membrane Science, 1988. **37**(2): p. 193-197.
42. Sano, T., et al., *Size-exclusion chromatography using self-organized nanopores in anodic porous alumina*. Applied Physics Letters, 2003. **83**(21): p. 4438-4440.
43. Mei, X., et al., *Molecular-beam epitaxial growth of GaAs and InGaAs/GaAs nanodot arrays using anodic Al₂O₃ nanohole array template masks*. Applied Physics Letters, 2002. **81**(2): p. 361-363.
44. Liang, J.Y., et al., *Two-dimensional lateral superlattices of nanostructures: Nonlithographic formation by anodic membrane template*. Journal of Applied Physics, 2002. **91**(4): p. 2544-2546.
45. Montero-Moreno, J.M., M. Sarret, and C. Muller, *Some considerations on the influence of voltage in potentiostatic two-step anodizing of AA1050*. Journal of

- the Electrochemical Society, 2007. **154**(3): p. C169-C174.
46. Fournier-Bidoz, S., et al., *Highly ordered nanosphere imprinted nanochannel alumina (NINA)*. *Advanced Materials*, 2004. **16**(23-24): p. 2193-+.
 47. Masuda, H., et al., *Highly ordered nanochannel-array architecture in anodic alumina*. *Applied Physics Letters*, 1997. **71**(19): p. 2770-2772.
 48. Tong, J.H., et al., *Preparation of a pinhole-free Pd-Ag membrane on a porous metal support for pure hydrogen separation*. *Journal of Membrane Science*, 2005. **260**(1-2): p. 84-89.
 49. Shu, J., et al., *Simultaneous Deposition of Pd and Ag on Porous Stainless-Steel by Electroless Plating*. *Journal of Membrane Science*, 1993. **77**(2-3): p. 181-195.
 50. Cheng, Y.S. and K.L. Yeung, *Palladium-silver composite membranes by electroless plating technique*. *Journal of Membrane Science*, 1999. **158**(1-2): p. 127-141.
 51. Xomeritakis, G. and Y.S. Lin, *Fabrication of a thin palladium membrane supported in a porous ceramic substrate by chemical vapor deposition*. *Journal of Membrane Science*, 1996. **120**(2): p. 261-272.
 52. Lee, C.H., et al., *Comparison of amperometric biosensors fabricated by palladium sputtering, palladium electrodeposition and Nafion/carbon nanotube casting on screen-printed carbon electrodes*. *Biosensors & Bioelectronics*, 2007. **22**(6): p. 877-884.
 53. Kudo, K., K. Kobayakawa, and Y. Sato, *Preparation of multilayered Co/Pd nanostructure films by electroplating and their magnetic properties*. *Electrochimica Acta*, 2001. **47**(1-2): p. 353-357.
 54. Chen, S.C., et al., *Preparation of palladium membrane by electroplating on*

AISI 316L porous stainless steel supports and its use for methanol steam reformer. Journal of Membrane Science, 2008. **314**(1-2): p. 5-14.

55. Cheng, F.L., et al., *Electrodeposited fabrication of highly ordered Pd nanowire arrays for alcohol electrooxidation.* Electrochemistry Communications, 2008. **10**(5): p. 798-801.
56. Xomeritakis, G. and Y.S. Lin, *Fabrication of thin metallic membranes by MOCVD and sputtering.* Journal of Membrane Science, 1997. **133**(2): p. 217-230.